



Cloud Atlas: Hubble Space Telescope Near-infrared Spectral Library of Brown Dwarfs, Planetary-mass Companions, and Hot Jupiters

Item Type	Article
Authors	Manjavacas, Elena; Apai, Dániel; Zhou, Yifan; Lew, Ben W. P.; Schneider, Glenn; Metchev, Stanimir A.; Miles-Páez, Paulo A.; Radigan, Jacqueline; Marley, Mark S.; Cowan, Nicolas B.; Karalidi, Theodora; Burgasser, Adam J.; Bedin, Luigi R.; Lowrance, Patrick J.; Kauffmann, Parker
Citation	Elena Manjavacas et al 2019 AJ 157 101
DOI	10.3847/1538-3881/aaf88f
Publisher	IOP PUBLISHING LTD
Journal	ASTRONOMICAL JOURNAL
Rights	© 2019. The American Astronomical Society. All rights reserved.
Download date	27/08/2022 17:12:36
Item License	http://rightsstatements.org/vocab/InC/1.0/
Version	Final published version
Link to Item	http://hdl.handle.net/10150/632420



Cloud Atlas: *Hubble Space Telescope* Near-infrared Spectral Library of Brown Dwarfs, Planetary-mass Companions, and Hot Jupiters

Elena Manjavacas¹ , Dániel Apai^{1,2,3} , Yifan Zhou¹ , Ben W. P. Lew⁴ , Glenn Schneider¹ , Stan Metchev⁵ ,
Paulo A. Miles-Páez^{1,5} , Jacqueline Radigan⁶, Mark S. Marley⁷ , Nicolas Cowan⁸ , Theodora Karalidi⁹ ,
Adam J. Burgasser¹⁰ , Luigi R. Bedin¹¹, Patrick J. Lowrance¹² , and Parker Kauffmann¹

¹Department of Astronomy/Steward Observatory, The University of Arizona, 933 N. Cherry Avenue, Tucson, AZ 85721, USA; elenamanjavacas@email.arizona.edu

²Department of Planetary Science/Lunar and Planetary Laboratory, The University of Arizona, 1629 E. University Boulevard, Tucson, AZ 85718, USA

³Earths in Other Solar Systems Team, NASA Nexus for Exoplanet System Science

⁴Department of Planetary Science/Lunar and Planetary Laboratory, The University of Arizona, 1640 E. University Boulevard, Tucson, AZ 85718, USA

⁵The University of Western Ontario, Department of Physics and Astronomy, 1151 Richmond Avenue, London, ON N6A 3K7, Canada

⁶Utah Valley University, 800 West University Parkway, Orem, UT 84058, USA

⁷NASA Ames Research Center, Mail Stop 245-3, Moffett Field, CA 94035, USA

⁸Department of Earth & Planetary Sciences, 3450 University St. Montreal, Quebec H3A 0E8, Canada

⁹Department of Astronomy and Astrophysics, University of California, Santa Cruz, California, USA

¹⁰Center for Astrophysics and Space Science, University of California San Diego, La Jolla, CA 92093, USA

¹¹INAF Osservatorio Astronomico di Padova, Vicolo Osservatorio 5, I-35122 Padova, Italy

¹²IPAC-Spitzer, MC 314-6, California Institute of Technology, Pasadena, CA 91125, USA

Received 2018 July 17; revised 2018 November 29; accepted 2018 December 7; published 2019 February 6

Abstract

Bayesian atmospheric retrieval tools can place constraints on the properties of brown dwarfs' and hot Jupiters' atmospheres. To fully exploit these methods, high signal-to-noise spectral libraries with well-understood uncertainties are essential. We present a high signal-to-noise spectral library (1.10–1.69 μm) of the thermal emission of 76 brown dwarfs and hot Jupiters. All our spectra have been acquired with the *Hubble Space Telescope*'s Wide Field Camera 3 instrument and its G141 grism. The near-infrared spectral types of these objects range from L4 to Y1. Eight of our targets have estimated masses below the deuterium-burning limit. We analyze the database to identify peculiar objects and/or multiple systems, concluding that this sample includes two very-low-surface-gravity objects and five intermediate-surface-gravity objects. In addition, spectral indices designed to search for composite-atmosphere brown dwarfs indicate that eight objects in our sample are strong candidates to have such atmospheres. None of these objects are overluminous, so their composite atmospheres are unlikely to be companion-induced artifacts. Five of the eight confirmed candidates have been reported as photometrically variable, suggesting that composite atmospheric indices are useful in identifying brown dwarfs with strongly heterogeneous cloud covers. We compare hot Jupiters and brown dwarfs in a near-infrared color–magnitude diagram. We confirm that the coldest hot Jupiters in our sample have spectra similar to mid-L dwarfs, and the hottest hot Jupiters have spectra similar to those of M-dwarfs. Our sample provides a uniform data set of a broad range of ultracool atmospheres, allowing large-scale comparative studies and providing an *HST* legacy spectral library.

Key words: brown dwarfs – stars: atmospheres

Supporting material: tar.gz file

1. Introduction

Over the past decade, increasingly detailed observations have become available for a wide range of objects: spectroscopic information is now available for hot Jupiters (e.g., Ranjan et al. 2014; Stevenson et al. 2014a; Line et al. 2016; Evans et al. 2017; Sheppard et al. 2017), directly imaged exoplanets (e.g., Rajan et al. 2017; Samland et al. 2017), and over a thousand brown dwarfs (e.g., Cushing et al. 2005; Kirkpatrick 2005; Burgasser et al. 2006; Apai et al. 2013; Buenzli et al. 2014; Schneider et al. 2015). These data sets have enabled major steps in the complexity and quantitative evaluation of atmospheric models. A particularly significant advancement has been the adaptation of a Bayesian modeling framework, first for hot Jupiters (e.g., Madhusudhan & Seager 2009; Line et al. 2013; Lee et al. 2014; Gandhi & Madhusudhan 2017; Fisher & Heng 2018; Pinhas et al. 2018) and smaller transiting planets (Benneke & Seager 2012), then for directly imaged exoplanets (Todorov et al. 2016; Lavie et al. 2017), and most recently for brown dwarfs (Line et al. 2015, 2017; Madhusudhan et al. 2016; Burningham et al. 2017).

The Bayesian modeling framework—although often less detailed than forward models—has two key advantages: first, it provides a probabilistic assessment of the fitted parameters and degeneracies, even if the parameter space is highly complex. Second, it enables systematic, comprehensive, unbiased modeling of large number of atmospheres, allowing for detailed comparative studies of the posterior distributions of the model parameters (e.g., C/O ratios, molecular abundances, surface gravities). Although the information provided by posterior distributions is very powerful, it must be remembered that the probabilities derived for individual model components are only correct under two related assumptions: that the data and uncertainties are correctly represented by the priors, and that the modeling framework itself is complete and correct. For example, data with hidden biases (resulting in incorrect priors) will yield systematically incorrect posteriors. In this sense, due to typical observational biases, it is particularly challenging to compare objects over a broad range of parameters (e.g., very different temperatures or surface gravities). In fact, no spectral library with well understood systematics exists for ultracool

atmospheres (hot Jupiters, directly imaged exoplanets, brown dwarfs). *In short, to exploit the potential of atmospheric retrievals and enable rigorous comparative studies of atmospheres, homogeneous spectral data sets with well-understood systematics are required.*

Comprehensive spectral libraries exist for brown dwarfs (Kirkpatrick et al. 1999, 2000; Leggett et al. 2000; Burgasser et al. 2002; McLean et al. 2003; Cushing et al. 2005; Kirkpatrick 2005; Burgasser et al. 2006, the SpeX spectral library,¹³ the Montreal spectral library,¹⁴ and references therein) built from ground-based spectroscopy of hundreds of brown dwarfs in dozens of studies. These libraries have played and continue to play essential roles in a broad range of brown dwarf studies. However, existing ground-based spectral libraries were built from data that are non-uniform in terms of instruments, observing conditions, and setups, as well as usually reduced slightly differently by different groups.

While these spectral libraries remain powerful, these data sets have several limitations for atmospheric retrieval studies: first, it is not possible to reliably capture the variety of differences in data acquisition, quality, and reduction with priors due to the unknowns involved. Second, ground-based observations unavoidably are influenced by telluric absorption, most notably by water bands. Although it is possible to correct for these to some extent, their time-varying nature and the optical depth in the bands lead to limited reliability in these bands. In fact, quantitative comparisons (D. Apai 2018, private communication) of some brown dwarfs with SpeX spectra and *Hubble Space Telescope* Wide Field Camera 3 near-infrared grism spectra revealed mismatches in water band shape and overall color (wavelength-dependent slope). We show these differences in Figure 1. In the left column, we show the direct comparison of the near-infrared SpeX (black) and *HST*/WFC3 spectra (blue) for randomly selected brown dwarfs with spectra in the SpeX and in our *HST*/WFC3 near-infrared library, and with spectral types between L5.5 and T6. In the right column, we show the ratio of the SpeX and the *HST*/WFC3 near-infrared spectra for the object in the left column. We show a green line indicating where a perfect match between the SpeX and the *HST*/WFC3 spectra should be (ratio Spex versus *HST*/WFC3 equal 1). In addition, we fit a line to the slope of the ratio between the two spectra, avoiding the water band at $1.4 \mu\text{m}$ (see black line), showing that in most of the cases, the slope is non-zero, indicating color trends on the SpeX spectra. In these plots, a common mismatch between the SpeX and the *HST*/WFC3 near-infrared spectra at the $1.4 \mu\text{m}$ water band is also evident, due to imperfect telluric correction. Given that the photometric precision and instrumental systematics of the *HST*/WFC3 instrument are very well understood, and that the *HST*/WFC3 near-infrared spectra are not affected by tellurics, the comparison reveals that low-level biases exist in the ground-based spectral libraries. While these corrections are well-suited for forward-modeling and object-to-object comparisons, they are often limiting for retrieval studies.

For example, Line et al. (2015) applied Bayesian atmospheric retrieval tools to SpeX spectra to derive thermal structures and molecular abundances of some brown dwarfs. Nevertheless, they

could only reach convergence in their Markov chain Monte Carlo retrievals if they assumed that the SpeX spectral uncertainties were underestimated. Thus, they artificially increased the SpeX spectral uncertainties that could reach a maximum of a factor of 100. In this case, it is impossible to disentangle if Line et al. (2015) models were incomplete, or if the uncertainties of the data sets were not accurately estimated and understood. Therefore, to properly test retrieval models, there is an obvious need for a uniform, space-based spectral library with well-understood spectral uncertainties.

In this paper, we present a high signal-to-noise spectral library with 76 near-infrared WFC3/*HST* spectra of brown dwarfs, low-mass companions to stars, and hot Jupiters. Our study supplements the *HST* Cloud Atlas Treasury program data (GO 14241, PI: D. Apai) with other published data sets (see Appendix A), carefully analyzing and correcting for (typically very small) data reduction differences. The advantage of the *HST*/WFC3 instrument is that it provides near-infrared spectroscopy ($1.10\text{--}1.69 \mu\text{m}$, S/N up to 3000 in the *J*-band) where the spectral energy distributions (SEDs) of these objects peak, and we observe the dominant absorbing species for brown dwarfs.

Aside from the presentation of our *HST*/WFC3 near-infrared spectral library, the goal of this study is to provide a comprehensive characterization of the objects of our sample. This spectral characterization is important to validate whether the results provided by the retrieval models match with the expectations for a given object. In fact, Line et al. (2015) used two well-characterized T dwarfs, Gl 570D and HD 3651B, to test their retrievals, thus confirming that the effective temperatures, surface gravities, masses, radii, etc., were consistent with the expected values for those T-dwarfs. Therefore, we aim to provide a basic characterization of our sample, and also to identify peculiar objects: extremely red or blue brown dwarfs, revealing low surface gravity or low metallicity objects; and overluminous brown dwarfs, potentially revealing multiple systems. In addition, we use spectral indices (Burgasser et al. 2006, 2010; Bardalez Gagliuffi et al. 2014) to search for spectral binaries. As a byproduct of this analysis, we found that these spectral indices can also be useful to search for variable brown dwarfs. In addition, we show the potential of our spectral library by performing a novel direct photometric and spectroscopic comparison between hot Jupiters and brown dwarfs, which can be only be accomplished at this level of accuracy with data acquired from the space. This comparison confirms that some hot Jupiters share effective temperatures and spectra with some M and L dwarfs.

In Section 2, we describe the targets that we include in the near-infrared *HST*/WFC3 spectral library. In Section 3, we derive spectral types for our sample using the SpeX Prism Spectral Library. In Section 4, we compare the L and T dwarfs with other brown dwarfs from Dupuy & Liu (2012) using a color–magnitude diagram (CMD). In Section 5, we search for low surface gravity objects in our sample using low surface gravity spectral indices. In Section 6, we search for composite atmosphere objects within our sample. In Section 7, we measure the water and methane bands on objects of our sample, in order to trace the change on the depth of those bands with the near-infrared spectral type. In Section 8, we directly compare colors and spectra of brown dwarfs and hot Jupiters in a CMD and find the best-matching brown dwarf for each of the hot Jupiters in our sample. Finally, we present our conclusions in Section 9.

¹³ The SpeX Prism Library is composed of low-resolution, near-infrared spectra, primarily of low-mass stars and brown dwarfs, obtained with the SpeX spectrograph mounted on the 3 m NASA Infrared Telescope Facility on Maunakea, Hawaii. The data provided here have been obtained using the prism-dispersed mode of SpeX with an average resolution of ~ 120 and spectra spanning $0.90\text{--}2.50 \mu\text{m}$: <http://pono.ucsd.edu/~adam/browndwarfs/spexprism/library.html>.

¹⁴ <https://jgagneastro.wordpress.com/the-montreal-spectral-library/>

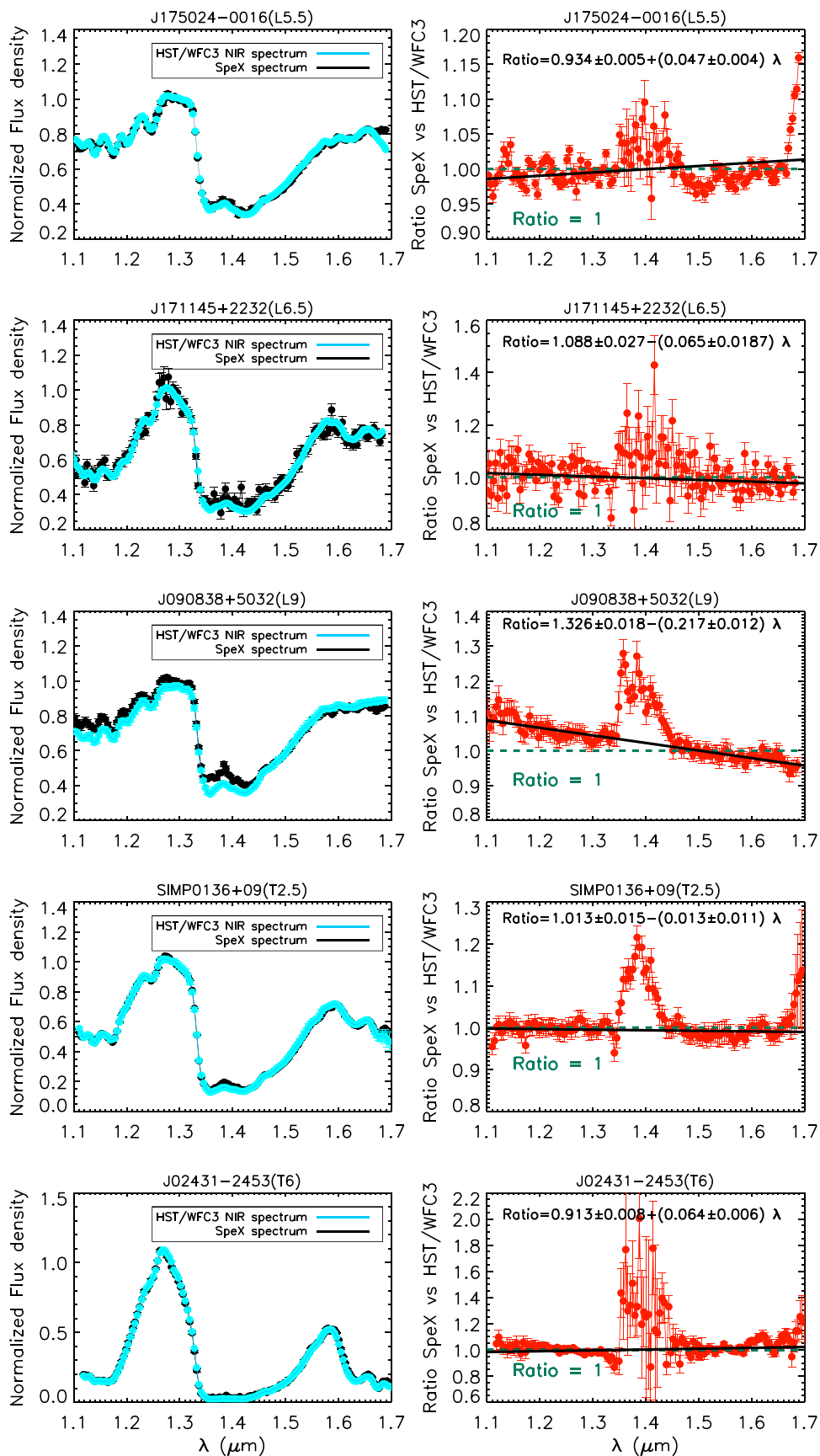


Figure 1. In the left column, we show a direct comparison between the SpeX and the *HST*/WFC3 near-infrared spectra. In the right column, we show the ratio between the SpeX and the *HST*/WFC3 near-infrared spectra. These plots reveal clear differences in the water band at 1.4 μm between both spectra, as well as color trends shown by non-zero slopes of the linear fits.

2. Targets

We compiled all spectra of brown dwarfs (including planetary-mass brown dwarfs; Caballero 2018), brown dwarf companions to stars, and hot Jupiter with emission spectra with published data from *HST*/WFC3 and its G141 grism (MacKenty et al. 2010). In addition, we present seven unpublished spectra observed as part of the *Cloud Atlas* treasury program (GO 14241, PI Apai), and other two brown dwarf spectra that belong to the *HST* program GO 13299 and 14051 (PI Radigan). These spectra cover the wavelength range between ~ 1.10 and $1.69 \mu\text{m}$, with a spectral resolving power $R = \frac{\lambda}{\Delta\lambda} = 130$ at $1.4 \mu\text{m}$. The image scale of WFC3/IR is 0.13 arcsec/pixel. In Tables 1 and 2 we provide the list of objects with names, celestial coordinates, and *HST* program identifiers in which the objects were observed, as well as the most relevant references in which this spectra were first published (Buenzli et al. 2012; Apai et al. 2013; Buenzli et al. 2014, 2015; Ranjan et al. 2014; Stevenson et al. 2014a, 2014b; Haynes et al. 2015; Peña Ramírez et al. 2015; Schneider et al. 2015; Yang et al. 2015, 2016; Lew et al. 2016; Line et al. 2016; Beatty et al. 2017; Cartier et al. 2017; Evans et al. 2017; Sheppard et al. 2017; Biller et al. 2018; Manjavacas et al. 2018; Zhou et al. 2018; and this work). In Table 1, for brown dwarfs and substellar companions, we specify their spectral types, Two Micron All Sky Survey (2MASS, Cutri et al. 2003) photometry, and trigonometric parallaxes, the signal-to-noise as measured at $1.25 \mu\text{m}$ from the corresponding *HST* programs, the *HST* program for which each object was observed, and the references in which these spectra were published. For hot Jupiters (Table 2), we also list the spectral types of the host stars, the star–planet separations, and the radii of the planets. In Figures 2–4, we show the spectra of the objects used in our study, 76 in total (22 L dwarfs, 28 T dwarfs, 16 Y dwarfs and 10 hot Jupiters), from which nine are presented here for the first time. Some of the objects in our sample in Table 1 have been classified as planetary-mass objects ($M < 13 M_{\text{Jup}}$). We list these objects in Table 3 along with their estimated masses, ages, young moving group membership (if known), and key references.

The observing log, including the observing dates, number of orbits per visit, exposure time of each single exposure, and the number of single exposures per orbit, is compiled in the Appendix.

The data sets and the data reduction by the authors that published the spectra presented in Tables 1 and 2 are described in Appendix A.

3. Spectral Types

The spectral types provided in column 3 of Table 1 for brown dwarfs and substellar companions are those given in the literature from the different sources. To provide a homogeneous spectral type classification, we compared our *HST*/WFC3 spectra to the spectra in the SpeX Prism Spectral Library. We compared our *HST*/WFC3 spectra using a modified χ^2 metric as presented in Cushing et al. (2008):

$$G = \sum_{\lambda} \left[\frac{C(\lambda) - \alpha T(\lambda)}{\sigma_c(\lambda)} \right]^2, \quad (1)$$

where $C(\lambda)$ is the spectrum of our object, $T(\lambda)$ is the comparison spectrum, α is a scaling factor that minimizes G , and $\sigma_c(\lambda)$ are the uncertainties of the spectrum. We additionally checked the best spectral matches by visual inspection.

In column 4 of Table 1, we show the resulting spectral types for each object. We found that the spectral types derived using the SpeX library are consistent with those published for each object in the literature, matching typically to within ± 1.5 spectral subtypes. The only exceptions are some of the known intermediate- or low-surface gravity objects in our sample. For these objects (CD-352722, LP 261-75b, 2MASS J2224438-015852, 2MASS J0310559+164816, S Ori 73), the difference in spectral types with respect to the literature values can be up to ± 3 spectral subtypes. These differences are expected, as the SpeX spectral library is mostly composed of field, i.e., high-surface-gravity brown dwarfs.

4. Color–Magnitude Diagrams

We use near-infrared CMDs for a simple-yet-quantitative comparison of the L and T brown dwarfs in this study to those published in Dupuy & Liu (2012), with the aim of identifying peculiar objects (extremely red or extremely blue dwarfs) or multiple systems. In Figure 5, we show the CMD plot, 2MASS $J - H$ color versus J -band absolute magnitude, for L and T brown dwarfs of Table 1 and objects from Dupuy & Liu (2012) as a comparison. We calculated the absolute J -band magnitude using trigonometric parallaxes, when available. Black stars represent objects from our sample listed in Table 1 with trigonometric parallaxes available in the literature. We do not include Y dwarfs in this CMD, as there are few other Y dwarfs for comparison. Red dots represent L dwarfs, green dots represent L-T brown dwarfs, and blue dots represent T dwarfs with trigonometric parallaxes published in Dupuy & Liu (2012). The solid gray line represents the color–absolute magnitude relationship for brown dwarfs, and the dotted gray line represents the rms (root mean square) of that relation.

The object 2MASS J00470038+6803543 (hereafter W0047, L7, object 9) stands out outside the rms of the color–absolute magnitude relation with red $J - H$ color index. Objects 2MASS J17503293+1759042 (hereafter 2M1750+1759, object 32) and 2MASS J05591914-1404488 (hereafter 2M0559-1404, object 34) are overluminous with respect to the other L-T transition objects, as they are above the rms of the color–magnitude relation for brown dwarfs (Dupuy & Liu 2012). The cause of their overluminosity is unknown, as no multiplicity has been reported previously for these objects.

5. Low Surface Gravity Objects

5.1. Gravity Index Determination

We use the low surface gravity indicators presented in Allers & Liu (2013) that are applicable to our sample up to spectral type L7. We aim to search for as of yet unidentified low surface gravity objects and to confirm those that previously have been classified as low surface gravity objects. Due to the spectral wavelength coverage of our *HST*/WFC3 spectra and their resolution, only the H -continuum and the KI_J indices are applicable to our spectra. The H -continuum measures the shape of the H -band, which has been found to be triangular for most of the very low-gravity brown dwarfs (< 100 Myr) with spectral types between M6 and L7. Intermediate and field gravity brown dwarfs show a “shoulder” at $1.57 \mu\text{m}$, indicative of the appearance of the FeH molecular absorption and the collisionally induced absorption by H_2 molecules (Borysow et al. 1997; Allard et al. 2012). Allers & Liu (2013) warned, though, that this index needs to be used in combination with others, as the

Table 1
Sample of L, T, and Y Dwarfs with *HST*/WFC3 Spectroscopy

Num.	Name	SpT	SpT _{SpeX} ^a	R.A. (J2000)	Decl. (J2000)	<i>J</i> (mag)	<i>H</i> (mag)	<i>K_s</i> (mag)	π_T (mas)	S/N ^b	<i>HST</i> GO ^c	Reference
1	CD-352722b	L4	L7.5	06 09 19.21	-35 49 31.20				44.63 ± 0.03	45	14241	TS
2	2MASS J17502484-0016151	L4.5	L5	17 50 24.84	-00 16 15.11	13.29 ± 0.02	12.41 ± 0.02	11.84 ± 0.02	45.16 ± 0.16	2000	12550	1, 13
3	2MASS J03552337+1133437	L5	L5.5	03 55 23.37	+11 33 43.70	14.05 ± 0.02	12.53 ± 0.03	11.53 ± 0.02	108.70 ± 2.36	322	14241	TS, 14
4	2MASS J18212815+1414010	L5	L5.5	18 21 28.15	+14 14 01.04	13.43 ± 0.02	12.39 ± 0.02	11.65 ± 0.02	122.00 ± 13.00	370	13176	2, 15
5	2MASSW J1507476-162738	L5	L5.5	15 07 47.69	-16 27 38.62	12.83 ± 0.03	11.89 ± 0.02	11.31 ± 0.02	106.50 ± 0.19	526	13176	2
6	2MASS J0421072-630602	L5	L5	04 21 07.19	-63 06 02.25	15.56 ± 0.05	14.28 ± 0.04	13.44 ± 0.04		1250	12550	1
7	2MASS J05395200-0059019	L5	L5	05 39 52.00	-00 59 01.90	14.03 ± 0.03	13.10 ± 0.03	12.52 ± 0.02	81.97 ± 2.69	2000	12550	1, 13
8	2MASS J1711457+223204	L5.0+T5.5		17 11 45.73	+22 32 04.41	17.08 ± 0.18	15.79 ± 0.11	14.72 ± 0.09	33.11 ± 4.71	1111	12550	1, 16
9	2MASS J00470038+6803543	L6	L5.5	00 47 01.06	+68 03 52.10	15.60 ± 0.07	13.97 ± 0.04	13.05 ± 0.03	82.00 ± 3.00	370	14241	3, 17
10	LP261-75B	L6	L4.5	09 51 04.60	+35 58 09.80	17.22 ± 0.21	15.89 ± 0.14	15.14 ± 0.13	29.60 ± 2.80	333	14241	4, 18
11	2MASS J01075242+0041563	L6	L5.5	01 07 52.42	+00 41 56.40	15.82 ± 0.06	14.51 ± 0.04	13.71 ± 0.04	64.13 ± 4.51	208	14241	TS, 19
12	2MASSW J1515008+484742	L6	L6	15 15 00.83	+48 47 41.69	14.11 ± 0.03	13.09 ± 0.03	12.50 ± 0.02		1666	12550	1, 20
13	2MASS J06244595-4521548	L6.5	L5	06 24 45.95	-45 21 54.89	14.48 ± 0.03	13.33 ± 0.03	12.59 ± 0.03	86.21 ± 4.46	1428	12550	1, 19
14	2MASSW J0801405+462850	L6.5	L6	08 01 40.56	+46 28 49.84	16.27 ± 0.13	15.45 ± 0.14	14.53 ± 0.10		1428	12550	1
15	PSO J318.5-22	L7	L7.5	21 14 08.03	-22 51 35.84	16.71 ± 0.19	15.72 ± 0.17	14.74 ± 0.12	45.10 ± 1.70	285	14188	10, 21
16	2MASSW J2224438-015852	L7.5	L4.5	22 24 43.82	-01 58 52.14	14.07 ± 0.03	12.81 ± 0.03	12.02 ± 0.02	86.20 ± 1.10	47	14241	2, 22
17	Luh 16AB	L7.5+T0.5		10 49 18.92	-53 19 10.08	11.5 ± 0.04	10.37 ± 0.04	9.44 ± 0.07	501.40 ± 0.09	500	13280	5, 23
18	2MASS J0825196+211552	L7.5	L6	08 25 19.69	+21 15 52.12	15.10 ± 0.03	13.79 ± 0.03	13.03 ± 0.03	93.46 ± 0.87	2000	12550	1, 24
19	2MUCD 10802	L8	L7.5	09 08 38.04	+50 32 08.82	14.55 ± 0.02	13.48 ± 0.03	12.95 ± 0.03		967	14241	1
20	2MASS J16322911+1904407	L8	L8	16 32 29.11	+19 04 40.71	15.86 ± 0.07	14.61 ± 0.04	14.00 ± 0.05	65.79 ± 2.16	1428	12550	1, 24
21	2MASSW J0310599+164816	L8	T2	03 10 59.87	+16 48 15.60	16.02 ± 0.08	14.93 ± 0.07	14.31 ± 0.07	36.90 ± 3.40	1428	12550	1, 16
22	2MASS J12195156+3128497	L9	L8	12 19 51.56	+31 28 49.71	15.91 ± 0.08	14.91 ± 0.07	14.31 ± 0.07		1428	12550	1
23	SDSS J075840.33+324723.4	T0+T3.5		07 58 40.03	+32 47 18.39	14.95 ± 0.04	14.11 ± 0.04	13.88 ± 0.06		3333	13299	TS
24	2MASS J10393137+3256263	T1	T2	10 39 31.38	+32 56 26.40	16.41 ± 0.15	15.34 ± 0.11	15.15 ± 0.16		1250	12550	1
25	2MASS J09090085+6525275	T1.5	T1	09 09 00.86	+65 25 27.57	16.03 ± 0.09	15.21 ± 0.09	15.17 ± 0.15		1250	12550	1
26	2MASS J21392676+0220226	T2	T1.5	21 39 26.77	+02 20 22.70	14.71 ± 0.01	14.16 ± 0.05	13.58 ± 0.04	101.50 ± 2.00	172	12314	11, 6, 25
27	2MASS J13243553+6358281	T2	T0.5	13 24 35.54	+63 58 28.15	15.59 ± 0.07	14.57 ± 0.06	14.05 ± 0.06		1111	12550	1, 6
28	2MASS J16291840+0335371	T2	T2	16 29 18.62	+03 35 35.01	15.29 ± 0.04	14.48 ± 0.03	14.04 ± 0.03		3333	14051	TS
29	HN PEG B	T2.5	T2.5	21 44 28.47	+14 46 07.80	15.86 ± 0.03	15.40 ± 0.03	15.12 ± 0.03	54.37 ± 0.85	2222	14241	9
30	SIMP J013656.5+093347.3	T2.5	T2.5	01 36 56.62	+09 33 47.30	13.46 ± 0.03	12.77 ± 0.03	12.56 ± 0.02	162.87 ± 1.06	370	12314	6, 11, 26
31	GU PSC B	T3.5	T1.5	01 12 36.48	+17 04 31.80				21.00 ± 0.07	100	14241	TS
32	2MASS J17503293+1759042	T3.5	T3.5	17 50 32.94	+17 59 04.30	16.34 ± 0.10	15.95 ± 0.13	15.48 ± 0.189	36.23 ± 4.46	909	12500	1, 16
33	2MASS J00001354+2554180	T4.5	T4.5	00 00 13.54	+25 54 18.10	15.06 ± 0.04	14.73 ± 0.07		14.84 ± 0.12	667	12550	1
34	2MASS J05591914-1404488	T4.5	T4.5	05 59 19.14	-14 04 48.88	13.80 ± 0.02	13.67 ± 0.04	13.57 ± 0.06	96.15 ± 0.96	833	12500	1, 22
35	2MASS J2339101+135230	T5.4	T5	23 39 10.25	+13 52 28.50	16.24 ± 0.11	15.82 ± 0.15	16.14 ± 0.31		909	12500	1
36	2MASS J1110100+0116130	T5.5	T5.5	11 10 09.99	+01 16 13.09	16.34 ± 0.12	15.92 ± 0.14	52.10 ± 1.20	52.10 ± 1.20	147	14241	TS, 27
37	2MASS J2228288-4310262	T6	T6	22 28 28.89	-43 10 26.27	15.66 ± 0.07	15.36 ± 0.12	15.29 ± 0.21	92.10 ± 2.60	243	12314	12, 6, 25
38	2MASS J0817300-6155158	T6	T6	08 17 30.01	-61 55 15.82	13.61 ± 0.02	13.53 ± 0.03	13.52 ± 0.04	204.08 ± 12.49	1000	12550	1, 19
39	S Ori 73	T4.5	T7.5	05 38 10.10	-02 36 26.00				5		12217	7
40	2MASS J0243137-245329	T6	T6	02 43 13.72	-24 53 29.80	15.38 ± 0.05	15.14 ± 0.11	15.22 ± 0.17	93.46 ± 3.49	667	12550	1, 22
41	2MASS J1624143+0029158	T6	T6	16 24 14.37	+00 29 15.82	15.49 ± 0.05	15.52 ± 0.10	11.00 ± 0.20	90.91 ± 1.65	909	12550	1, 28
42	CFBDSIR2149-0403	T7		21 49 47.20	-04 03 08.90				18.30 ± 1.80	6.7	14241	TS, 29
43	S Ori 70	T7	T7.5	05 38 14.19	-02 45 11.80	20.91 ± 0.07	20.83 ± 0.12	20.91 ± 0.15		5	12217	7
44	ROSS458C	T8	T7.5	13 00 41.94	+12 21 14.72	16.68 ± 0.01	17.01 ± 0.04	16.89 ± 0.06	85.54 ± 1.53	65	14241	TS
45	WISEA J032504.5-504403.0	T8		03 25 04.52	-50 44 03.00	18.43 ± 0.26	16.21 ± 0.15	>12.918		8	13178	8
46	WISEA J033515.1+431044.7	T9		03 35 15.07	+43 10 44.70	>18.652			14.52 ± 0.06	5	12970	8
47	WISEA J040443.5-642030.0	T9		04 04 43.50	-64 20 30.00	18.44 ± 0.18	15.73 ± 0.06	>12.297		23	13178	8
48	WISEA J221216.3-693121.6	T9		22 12 16.27	-69 31 21.60	17.26 ± 0.12	14.87 ± 0.06	>12.278		4	12970	8

Table 1
(Continued)

Num.	Name	SpT	SpT _{SpeX} ^a	R.A. (J2000)	Decl. (J2000)	<i>J</i> (mag)	<i>H</i> (mag)	<i>K_s</i> (mag)	π_T (mas)	S/N ^b	<i>HST</i> GO ^c	Reference
49	WISEA J094306.0+360723.3	T9.5		09 43 05.99	+36 07 23.57	19.74 ± 0.05	20.37 ± 0.20			2	12970	8
50	WISEA J154214.0+223005.2	T9.5		15 42 14.00	+22 30 05.20	20.25 ± 0.13	21.80 ± 0.80	96.00 ± 41.00		2	12230	8, 27
51	WISEA J035934.1–540154.8	Y0		03 59 34.07	–54 01 54.80	>19.031		15.38 ± 0.05	75.40 ± 6.62	2	12970	8, 34
52	WISEA J041022.8+150247.9	Y0		04 10 22.75	+15 02 47.90	>18.170		14.11 ± 0.05	153.40 ± 4.00	2	12970	8, 34
53	WISEA J073444.0–715743.8	Y0		07 34 44.03	–71 57 43.80	20.13 ± 0.08			67.60 ± 8.70	2	12970	8, 34
54	WISEA J120604.3+840110.5	Y0		12 06 04.38	+84 01 10.60	>18.734		15.06 ± 0.05	85.10 ± 9.30	2	13178	8, 34
55	WISE J154151.7–225024.9	Y0		15 41 51.66	–22 50 24.99	20.99 ± 0.03	20.99 ± 0.52		167.10 ± 4.20	2	12970	8, 34
56	WISEA J173835.5+273258.8	Y0		17 38 35.53	+27 32 59.10	19.47 ± 0.08	20.39 ± 0.33		128.50 ± 6.30	2	12230	8, 34
57	WISEA J205628.9+145953.6	Y0		20 56 28.92	+14 59 53.22	16.48 ± 0.07	13.84 ± 0.04	11.73 ± 0.25	138.30 ± 3.90	5	12230	8, 34
58	WISEA J222055.3–362817.5	Y0		22 20 55.32	–36 28 17.50	>18.772		14.71 ± 0.06	84.10 ± 5.90	3	12970	8, 34
59	WISEA J220905.8+271143.6	Y0:		22 09 05.73	+27 11 44.00	22.58 ± 0.14	22.98 ± 0.31	154.40 ± 5.70		1	12970	8, 34
60	WISEA J082507.4+280548.2	Y0.5		08 25 07.36	+28 05 48.56	>18.444		14.58 ± 0.06	139.00 ± 4.30	1	12970	8, 34
61	WISEA J140518.3+553421.3	Y0.5		14 05 18.39	+55 34 21.40	21.06 ± 0.06	21.45 ± 0.41		144.30 ± 8.60	1	12230	8, 34
62	WISEA J163940.8–684739.4	Y0pec		16 39 40.83	–68 47 38.60	20.57 ± 0.05			228.10 ± 8.90	5	12970	8, 34
63	WISEA J053516.9–750024.6	Y1		05 35 16.87	–75 00 24.60	17.94 ± 0.14	14.90 ± 0.05	>12.349	79.50 ± 8.80	1	12970	8, 34
64	WISEA J035000.3–565830.5	Y1		03 50 00.31	–56 58 30.50	>18.699		14.74 ± 0.04	168.80 ± 8.50	1	12230	8, 34
65	WISEA J064723.2–623235.4	Y1		06 47 23.24	–62 32 35.40	22.45 ± 0.07			83.70 ± 5.70	1	12970	8, 34
66	WISEA J235402.8+024014.1	Y1		23 54 02.79	+02 40 14.10	>18.263		15.01 ± 0.09		1	13178	8

Notes. References for first publication of *HST*/WFC3 near-infrared spectra: TS—This study; (1) Buenzli et al. (2014); (2) Yang et al. (2015); (3) Lew et al. (2016); (4) Manjavacas et al. (2018); (5) Buenzli et al. (2015); (6) Yang et al. (2016); (7) Peña Ramírez et al. (2015); (8) Schneider et al. (2015); (9) Zhou et al. (2018); (10) Biller et al. (2018); (11) Apai et al. (2013); (12) Buenzli et al. (2012). References for trigonometric parallax measurements: (13) Andrei et al. (2011); (14) Faherty et al. (2013); (15) Sahlmann et al. (2016); (16) Vrba et al. (2004); (17) Gizis et al. (2015); (18) Liu et al. (2016); (19) Faherty et al. (2012); (20) Wang et al. (2018); (21) Liu et al. (2013); (22) Dupuy & Liu (2012); (23) (Bedin et al. 2017); (24) Dahn et al. (2002); (25) Marocco et al. (2013); (26) Weinberger et al. (2013); (27) Tinney et al. (2014); (28) Tinney et al. (2003); (29) Delorme et al. (2017); (30) Marsh et al. (2013); (31) Luhman & Esplin (2016); (32) Kirkpatrick et al. (2011); (33) Leggett et al. (2017); (34) Martin et al. (2018).

^a SpT_{SpeX}^a is the spectral type of each the spectra compiled in this work derived by comparison to the SpeX Prism Spectral Library.

^b S/N measured at 1.25 μm .

^c Further details of the program-specific observation plan can be found at: <http://www.stsci.edu/cgi-bin/get-proposal-info?id=#####&submit=Go&observatory=HST>, where ##### should be replaced by the given GO program number.

Table 2
Sample of Hot Jupiters with *HST*/WFC3 Spectroscopic Data

Num.	Name	R.A.	Decl.	SpT Host	π_T^a (mas)	Separation (au)	Planet Radius (R_{Jup})	S/N ^b	<i>HST</i> Prog.	Reference
67	WASP-18b	01 37 25.03	−45 40 40.39	F6V	7.91 ± 0.30	0.02014 ± 0.00034	1.165 ± 0.077	37.8	13467	9
68	WASP-33b	02 26 51.06	+37 33 01.73	A5	8.51 ± 0.24	0.02555 ± 0.00043	1.497 ± 0.045	38.9	12495	2
69	HD 209458B	22 03 10.77	+18 53 03.54	G0V	20.47 ± 0.02	0.04723 ± 0.00079	1.359 ± 0.015	6.4	13467	1
70	WASP-12b	06 30 32.79	+29 40 20.29	G0V	2.57 ± 0.27	0.02253 ± 0.00038	1.790 ± 0.090	12.3	13467	4
71	WASP-121b	07 10 24.06	−39 05 50.55	F6V	3.82 ± 0.25	0.02544 ± 0.00050	1.865 ± 0.044	13.3	14767	8
72	WASP-43b	10 19 38.01	−09 48 22.59	K7V	11.49 ± 0.04	0.01424 ± 0.00041	0.930 ± 0.070	12.5	13467	7
73	WASP-103b	16 37 15.57	+07 11 00.07	F8V	2.13 ± 0.16	0.01987 ± 0.00033	1.528 ± 0.073	8.3	14050	3
74	TrES-3b	17 52 07.02	+37 32 46.18	K0V	4.29 ± 0.02	0.02272 ± 0.00038	1.336 ± 0.031	2.5	12181	5
75	Kepler-13Ab	19 07 53.15	+46 52 05.91	A0	1.91 ± 0.01	0.04171 ± 0.00078	1.406 ± 0.038	10.8	13308	6
76	WASP-4b	23 34 15.08	−42 03 41.14	G7V	3.63 ± 0.70	0.02304 ± 0.00042	1.341 ± 0.023	4.4	12181	5

Notes.

^a Trigonometric parallaxes delivered by Gaia Collaboration et al. (2018).

^b The S/N is measured between 1.05 and 1.65 μm .

References. (1) Line et al. (2016); (2) Haynes et al. (2015); (3) Cartier et al. (2017); (4) Stevenson et al. (2014a); (5) Ranjan et al. (2014); (6) Beatty et al. (2017); (7) Stevenson et al. (2014b); (8) Evans et al. (2017); (9) Sheppard et al. (2017).

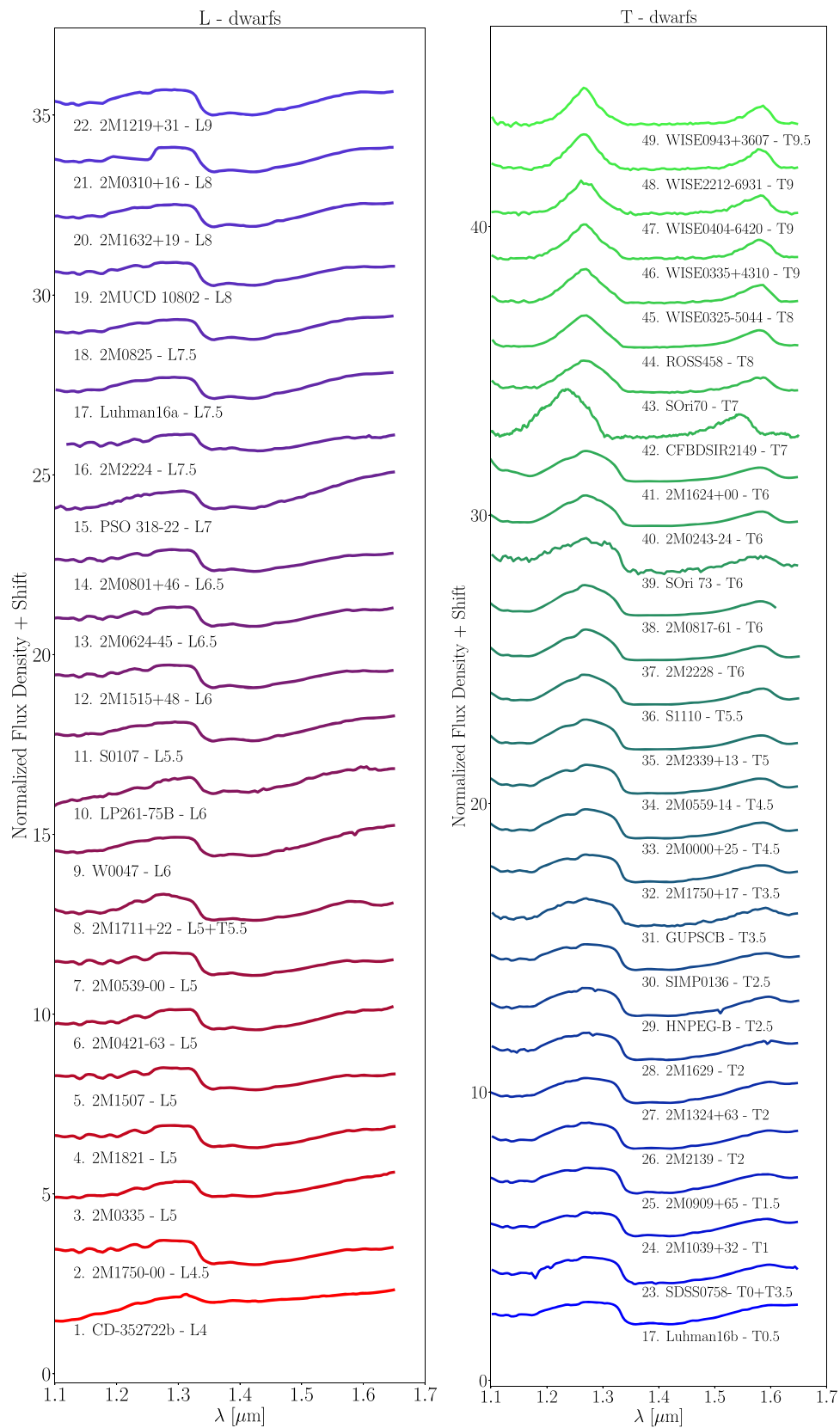


Figure 2. L and T dwarfs with *HST*/WFC3 spectra used as a part of this study. Flux is normalized at $1.25 \mu\text{m}$.

H-band is also triangular for some objects that do not have low surface gravity. The KI_J index measures the alkali line doublet depth at 1.244 and $1.253 \mu\text{m}$. These have been found to be

weaker for low surface gravity objects of spectral types between M5 to L7. The continuum, center, and bandwidth of these indices are described in Table 4. Their values are

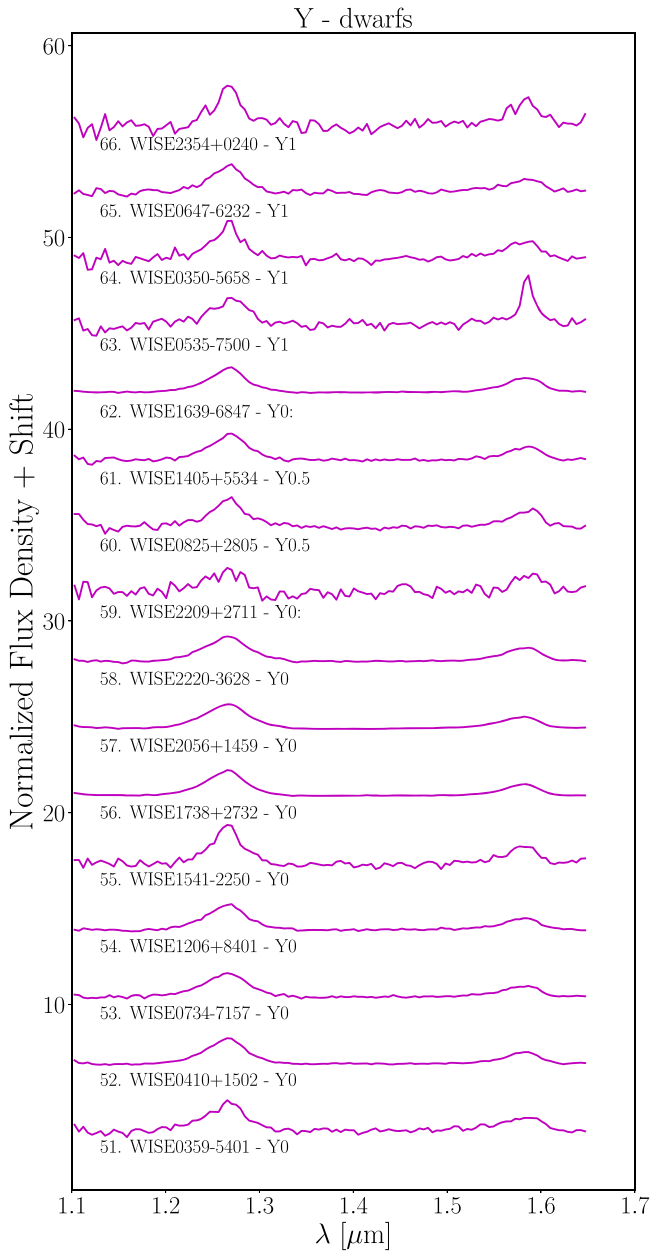


Figure 3. Y dwarfs with *HST*/WFC3 spectra used as a part of this study. Flux is normalized at $1.25 \mu\text{m}$.

calculated using Equation (1) from Allers & Liu (2013). Different values for the KI_J and H -continuum indices correspond to different gravity scores: 0, 1 and 2, corresponding to field gravity (FLD-G), intermediate (INT-G), or low surface gravity objects (VL-G), respectively. The ranges of values of the KI_J and the H -continuum indices that correspond to different gravity scores are given in Table 9 of Allers & Liu (2013). The KI_J and the H -continuum indices and their gravity scores obtained for our objects are shown in Table 5. In Figure 6, we show the spectral type versus the KI_J and the H -continuum indices for our sample (up to L7 spectral type) and for objects that belong to young moving groups, γ and β dwarfs¹⁵, young companions (Allers & Liu 2013;

¹⁵ Optical classification for very low and intermediate surface gravity, respectively (Cruz et al. 2009).

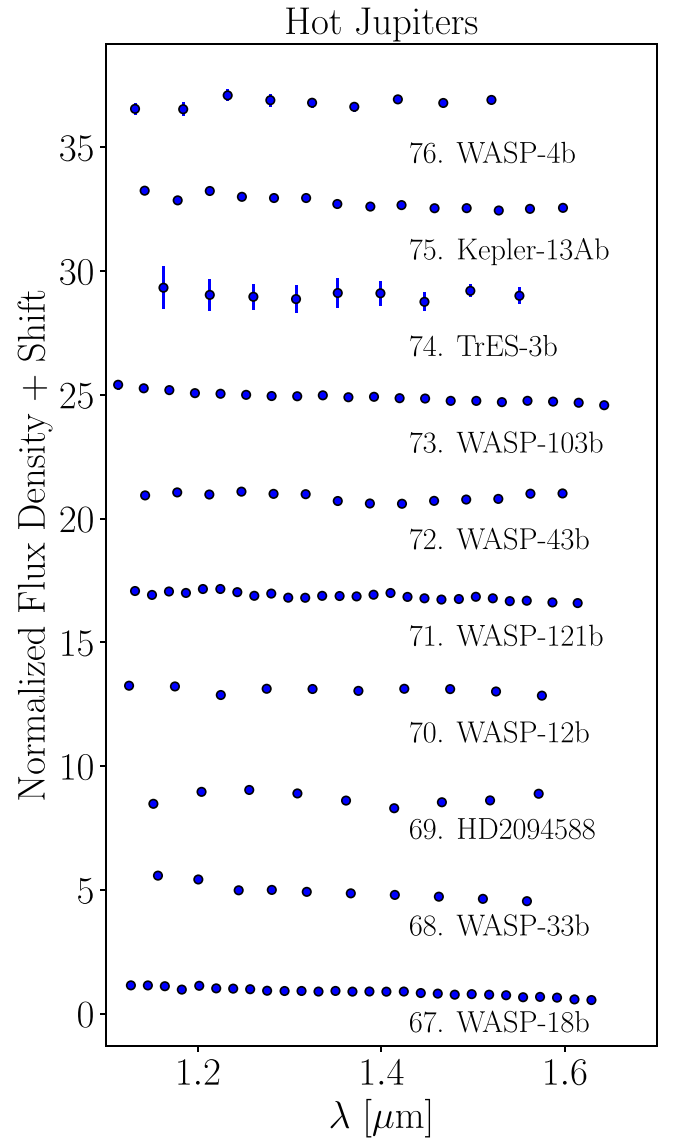


Figure 4. Hot Jupiters with *HST*/WFC3 emission spectra used as a part of this study. Some error bars are smaller than the symbol for the measurement.

Bonnefoy et al. 2014), and field brown dwarfs (McLean et al. 2003; Cushing et al. 2005), for comparison.

5.2. Results: Gravity Class Determination

Among the 16 objects in our sample with spectral types up to L7 for which the KI_J and the H -continuum indices could be measured, two have gravity scores consistent with very low surface gravities: CD-352722B (object 1) and 2MASS J03552337+1133437 (object 3). Five objects had gravity scores consistent with intermediate gravities: 2MASSI J0421072–630602 (object 6), 2MASS J00470038+6803543 (object 9), 2MASS J01075242+0041563 (object 11), PSO J318.5–22 (object 15), and 2MASSW J2224438–015852 (object 16).

CD-352722B and 2MASS J03552337+1133437 had been reported before as low surface gravity objects by Wahhaj et al. (2011) and Faherty et al. (2013), respectively, and they are also high-probability members of the AB-Doradus moving group with an estimated age of ~ 120 Myr (Zuckerman et al. 2004).

Table 3
Age and Mass Estimates for the Planetary-mass Objects of Our Sample

Num.	Name	SpT	Mass (M_{Jup})	Age (Myr)	YMG	Reference
3	2MASS J03552337+1133437	L5.0	13–30	~ 120	AB-Doradus	1
9	2MASS J00470038+6803543	L6.0	20^{+3}_{-7}	~ 120	AB-Doradus	2
15	PSO J318.5–22	L7.0	8.3 ± 0.5	23 ± 3	β -Pic	3, 4
30	SIMP J013656.5+093347.3	T2.5	12.7 ± 1.0	~ 120	AB-Doradus	5
31	GU PSC B	T3.5	$11.9^{+2}_{-1.5}$	~ 120	AB-Doradus	2
36	2MASS J11101001+0116130	T5.5	10–12	~ 120	AB-Doradus	6
42	CFBDSIR2149–0403	T7.0	2–13	< 500	None	7
44	ROSS458C	T8.0	5–20	< 1000	None	8

References. (1) Faherty et al. (2013); (2) Aller et al. (2016); (3) Liu et al. (2013); (4) Allers et al. (2016); (5) Gagné et al. (2017); (6) Gagné et al. (2015a); (7) Delorme et al. (2017); (8) Burningham et al. (2011).

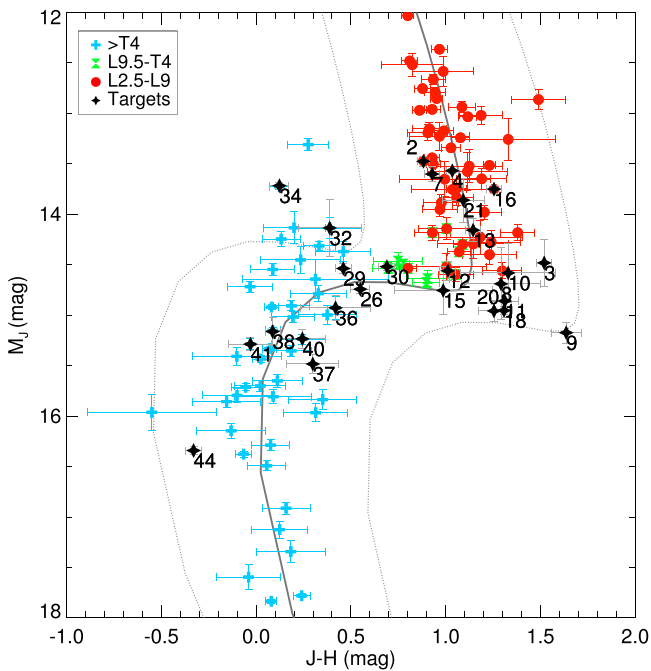


Figure 5. 2MASS $J - H$ color vs. M_J 2MASS absolute magnitude diagram. The black stars correspond to L and T dwarfs of our sample with measured trigonometric parallaxes published in the literature. Red dots are L dwarfs, green dots are L-T transitions dwarfs, and blue dots are T dwarfs with parallaxes published in Dupuy & Liu (2012). The solid gray lines represent the color-absolute magnitude relationships for brown dwarfs. The dotted gray lines represent the rms of that relation. Objects lying outside the rms of the relation, are cataloged extremely red, extremely blue, or overluminous.

Object 2MASS J0421072–630602 (object 6) was classified as an intermediate-surface gravity ($L5\beta$) object by Cruz et al. (2009) in optical wavelengths.

2MASS J00470038+6803543 (object 9) is an extremely red L-dwarf, and a bona fide member of the AB Doradus moving group, for which intermediate surface gravity characteristics have been previously reported (Gizis et al. 2012; Allers & Liu 2013).

PSO J318.5–22 is also an extremely red L-dwarf for which low surface gravity signatures have been found (Liu et al. 2013) and is a bona fide member of the β -Pictoris moving group, with age = 23 ± 3 Myr (Zuckerman et al. 2001; Mamajek & Bell 2014).

Object 2MASS J01075242+0041563 (object 11) does not clearly show low surface gravity spectral characteristics (Gagné et al. 2015b), and it was found to be a possible member

Table 4
Spectral Indices to Segregate Young Brown Dwarfs from Allers & Liu (2013)

Index	λ_{line} (μm)	λ_{cont1} (μm)	λ_{cont2} (μm)	Width in λ
KI _J	1.244	1.220	1.270	0.0166
H-cont	1.560	1.470	1.670	0.0208

of the Hyades association, with age ~ 625 Myr (Bannister & Jameson 2007). If confirmed, its age would not be consistent with its intermediate gravity classification (expected for objects with ages between 50 and 200 Myr; see Allers & Liu (2013)).

Finally, 2MASSW J2224438–015852 (object 16) is an extremely red L4.5 dwarf that was classified as a field dwarf by Liu et al. (2016) using the BANYAN II tool. Martin et al. (1996) classified it as a field gravity object using NIRSPEC/Keck II spectra to obtain Allers & Liu (2013) indices in the J -band.

6. Candidates for Composite Atmospheres

Our high-quality spectra are well-suited for exploring the diversity of ultracool atmospheres, including the identification of potentially composite (multicomponent) spectra. Obvious sources of such composite spectra are unresolved binaries with different spectral types. However, given the very high occurrence rate of heterogeneous cloud cover in brown dwarfs (Buenzli et al. 2014; Metchev et al. 2015), it is expected that brown dwarfs with strong spectral heterogeneity will also contribute to the population of composite atmospheres.

6.1. Search for Composite Atmosphere Brown Dwarfs

To identify potential composite spectra candidates in our sample, we used the spectral indices from Burgasser et al. (2006, 2010) and Bardalez Gagliuffi et al. (2014). These indices examine peculiar spectral characteristics of spectroscopic L-plus-T and M-plus-T composite atmosphere brown dwarfs. L plus T composite spectra have bluer SEDs in the near-infrared than field objects of similar spectral type. In cases of L-plus-T spectroscopic binaries, atomic and molecular features are blended, affecting the H_2O ($1.15 \mu\text{m}$) and CH_4 ($1.32 \mu\text{m}$) molecular features. At $1.55 \mu\text{m}$, spectroscopic L+T binaries show larger flux from the T dwarf. Burgasser et al. (2006, 2010) and Bardalez Gagliuffi et al. (2014) combine different pairs of indices, more efficiently defining those that segregate brown dwarfs with composite spectra.

The criteria to select potential brown dwarf composite atmospheres, along with the delimiters of the areas within the plots comparing different indices that segregate spectroscopic

Table 5
Values Obtained for the H -continuum and KI_J Indices for Our Objects, with their Corresponding Gravity Scores

Object	Name	H -continuum	KI_J	Gravity Score per Index	Gravity Class
1	CD-352722B	1.028 ± 0.001	1.013 ± 0.001	2 2	VL-G
2	2MASS J17502484-0016151	0.829 ± 0.001	1.106 ± 0.001	0 0	FLD-G
3	2MASS J03552337+1133437	0.982 ± 0.001	1.046 ± 0.001	2 2	VL-G
4	2MASS J18212815+1414010	0.867 ± 0.001	1.101 ± 0.001	0 0	FLD-G
5	2MASSW J1507476-162738	0.829 ± 0.001	1.109 ± 0.001	0 0	FLD-G
6	2MASSI J0421072-630602	0.892 ± 0.001	1.070 ± 0.001	1 1	INT-G
7	2MASS J05395200-0059019	0.806 ± 0.001	1.109 ± 0.001	0 0	FLD-G
8	2MASSI J1711457+223204	0.734 ± 0.001	1.052 ± 0.001	0...	FLD-G
9	2MASS J00470038+6803543	0.934 ± 0.001	1.006 ± 0.001	1...	INT-G
10	LP261-75B	0.713 ± 0.004	1.076 ± 0.001	0 1	FLD-G
11	2MASS J01075242+0041563	0.883 ± 0.001	1.015 ± 0.001	1 2	INT-G
12	2MASSW J1515008+484742	0.809 ± 0.001	1.072 ± 0.001	0...	FLD-G
13	2MASS J06244595-4521548	0.839 ± 0.001	1.086 ± 0.001	0 1	FLD-G
14	2MASSW J0801405+462850	0.869 ± 0.001	1.059 ± 0.001	0...	FLD-G
15	PSO J318.5-22	0.918 ± 0.002	0.982 ± 0.001	1...	INT-G
16	2MASSW J2224438-015852	0.898 ± 0.001	1.084 ± 0.001	1 1	INT-G

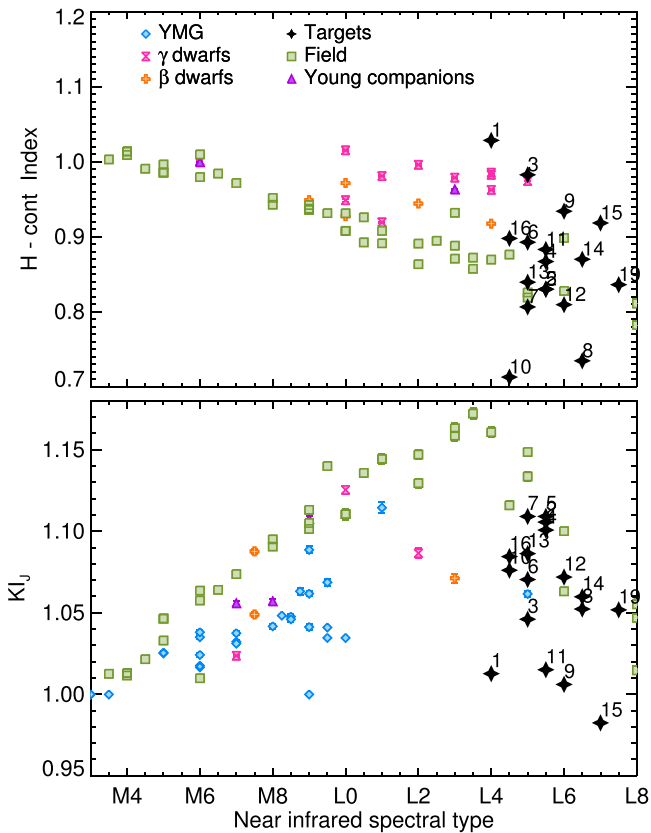


Figure 6. Spectral types vs. H -continuum and KI_J indices from Allers & Liu (2013). For comparison, we show the value of these indices of the field (green squares), young companions (purple triangles), β dwarfs (intermediate surface gravity; orange crosses), γ dwarfs (very low gravity; pink hourglass symbol) and young moving group members (blue diamonds). Black stars belong to objects of the sample presented in this work with spectral types between L3 and L7. Numbers identify the objects from Table 1.

brown dwarfs with composite spectra, are defined in the Appendix. We do not measure indices that are outside the wavelength range of the $HST/WFC3$ G141 near-infrared spectra. Thus, only 13 out of 18 available plots comparing indices from Burgasser et al. (2006, 2010) and Bardalez Gagliuffi et al. (2014) are applicable to our data (see the tables

in the Appendix). In the figures in the Appendix, we show a comparison of the spectral indices listed in the tables in the Appendix. To be considered a weak candidate to have a composite brown dwarf atmosphere, Burgasser et al. (2006, 2010) and Bardalez Gagliuffi et al. (2014) established that an object needs to appear within the selection area of at least four plots, and to be considered a strong candidate, it needs to appear at least in eight plots. Due to the wavelength coverage of the $HST/WFC3$ data, we were not able to perform five of the index comparisons in Burgasser et al. (2006, 2010) and Bardalez Gagliuffi et al. (2014), but we conservatively use the same criteria to select weak and strong spectroscopic binaries.

6.2. Results: Composite Atmosphere Candidates

We found that ten objects in our sample were selected by the indices as weak composite spectra candidates: 2M0310+16 (object 21), 2M0624-45 (object 13), 2MUCD 10802 (object 19), 2M0909+65 (object 25), 2M1039+32 (object 24), 2M1324+63 (object 27), 2M1515+48 (object 12), 2M1632+19 (object 20), 2M1711+22 (object 8), 2M1750-00 (object 2). In addition, we found three strong candidates to have composite spectra: 2M1507-16 (object 5), 2M1219+31 (object 22), and SIMP0136+09 (object 30).

To confirm or reject the candidates, we compared our $HST/WFC3$ spectra to single template spectra from the SpeX Prism Spectral Library, and independently, to synthetic L plus T composite spectra created using single spectra from those libraries (see Table 6). To create the synthetic composite spectra, we scaled the fluxes of the components to 10 pc using the color-magnitude relation from Dupuy & Liu (2012), and coadded the two component fluxes.

Following Burgasser et al. (2006, 2010) and Bardalez Gagliuffi et al. (2014), we compared the goodness of the fit of the $HST/WFC3$ spectra to the single, and independently, to synthetic L plus T composite spectra using a modified χ^2 (G) using Equations (1) from Cushing et al. (2008).

Finally, we tested if the fit to a composite template spectra was significantly better than the fit to a single template using a one-sided F-test statistic. The distribution statistic ratio we used

Table 6
Candidates for Composite Spectra Selected by Burgasser et al. (2006, 2010) and Bardalez Gagliuffi et al. (2014) Spectral Indices

Num.	Name	SpT	Single Component	Binary Components	η_{SB}	Variable?
21	2M0310+16	L8	L8 (SD J121951.45+312849.4)	(L8) SD J085758.45+570851.4 + T0 (SD J042348.57-041403.5)	1.27	Yes (1)
13	2M0624-45	L6.5	L5 (2M J23512200+3010540)	L3.5 (2M J2224438-015852) + T1 (SD J163239.34+415004.3)	2.18	Yes (1)
19	2MUCD 10802	L7.5	L7.5 (SD J115553.86+055957.5)	L7.5 (SD J115553.86+055957.5) + T0 (GI337CD)	1.43	No (1)
25	2M0909+65	T1.5	T2 (2M J11220826-3512363)	L9.5 (SD J082030.12+103737.0) + T3.5 (SD J175032.96+175903.9)	1.03	No (1)
24	2M1039+32	T1	T1.5 (SD J090900.73+652527.2)	L8 (SD J121951.45+312849.4) + T4 (2M J2254188+312349)	3.25	Yes (1)
22	2M1219+31	L8	L8 (2M J0328426+230205)	L9 (2M J0310599+164816) + T0 (GI 337CD)	2.07	Yes (1)
27	2M1324+63	T2	T2 (SD J125453.90-012247.4)	L9 (SD J083008.12+482847.4) + T7.5 (2M J11145133-2618235)	3.94	Yes (1)
12	2M1515+48	L6	L9 (2M J0908380+503208)	L9 (2M J0908380+503208) + T0 (SD J152039.82+354619.8)	1.69	No (1)
20	2M1632+19	L8	L8 (GI584C)	L6(2M J0825196+211552)+T0(SD J204749.61-071818.3)	2.71	Yes (1)
8	2M1711+22	L5.0+T5.5	T1 (SD J085834.42+325627.7)	L6(2M J0825196+211552)+T3(SD J102109-030420)	2.30	Binary
2	2M1750-00	L5.5	L5 (2M J18131803+5101246)	L4.5 (2M J15200224-4422419B) + T0.5 (SD J151643.01+305344.4)	0.79	Yes(1)
5	2M1507-16	L5.5	L5 (2M J17461199+5034036)	L5 (2M J10461875+4441149) + T0 (2M J0920122+351742)	1.18	Yes (2)
30	SIMP0136+09	T2.5	T2 (2MASS J11220826-3512363)	SD J213154.43-011939.3 (L9) + SD J092615.38+584720.9 (T4.5)	0.95	Yes (3)

References. (1) Buenzli et al. (2014); (2) Yang et al. (2015); (3) Artigau et al. (2009).

Table 7
Photometric Variability Reported for Final Weak and Strong Candidates for Composite Spectra

Num.	Name	SpT principal component	Variable?	π_{Trig} (mas)	M_J (mag)	$M_{J,\text{SP}}^a$ (mag)
13	2M0624-45	L6.5	Yes (1)	86.21 ± 4.46	14.16 ± 0.12	14.11 ± 0.40
19	2MUCD 10802	L7.5	No (1)
24	2M1039+32	T1	Yes (1)
22	2M1219+31	L8	Yes (1)
27	2M1324+63	T2	Yes (1)
12	2M1515+48	L6	No (4)	123.8 ± 5.0	14.56 ± 0.09	13.94 ± 0.40
20	2M1632+19	L8	Yes (2)	65.19 ± 2.16	14.96 ± 0.10	14.51 ± 0.40
8	2M1711+22	L6.5	Binary (3)	33.11 ± 4.71	14.69 ± 0.36	14.11 ± 0.40

Note.

^a Absolute magnitude given by the empirical spectro-photometric relation by Dupuy & Liu (2012).

References. (1) Buenzli et al. (2014); (2) Metchev et al. (2015); (3) Burgasser et al. (2010); (4) Bardalez Gagliuffi et al. (2014); (5) Artigau et al. (2009); (6) Yang et al. (2015).

was:

$$\eta_{\text{SB}} = \frac{\min(G_{\text{single}}) \times df_{\text{composite}}}{\min(G_{\text{composite}}) \times df_{\text{single}}} \quad (2)$$

where $\min(G_{\text{single}})$ and $\min(G_{\text{composite}})$ are the minimum G for the best match to a single or a composite template, and $df_{\text{composite}}$ and df_{single} are the degrees of freedom for the composite template spectra fit and the single template fit. The degrees of freedom are the number of data points used in the fit minus one, to account the scaling between our spectra and the template spectra. To rule out the null hypothesis, meaning that the candidate spectrum is not best described by a single template at the 99% confidence level, we require $\eta_{\text{SB}} > 1.41$. The F-statistic analysis rejected five of our candidates: 2M0310+16 (object 21), 2M0909+65 (object 25), 2M1750-00 (object 2), 2M1507-16 (object 5), and SIMP0136+09 (object 30).

Unresolved binaries should appear overluminous compared to single brown dwarfs. To test for evidence of overluminosity in our targets, we compared the absolute magnitudes, derived using the trigonometric parallaxes for our targets, with the spectro-photometric absolute magnitudes derived using the relation published by Dupuy & Liu (2012) (see Table 7). To obtain spectro-photometric absolute magnitudes, we used the spectral type of the principal component. We found that none of the sources with trigonometric parallaxes are overluminous. Actually, we find that some of them are slightly underluminous. This fact does not support the multiplicity hypothesis.

6.3. Rotational Modulation and Composite Atmosphere Candidates

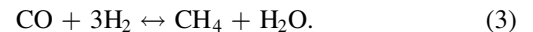
We also searched for published rotational modulation detections for our candidates as a potential marker for composite atmospheres. We found that nine of the thirteen composite atmosphere candidates have reported photometric variability due to cloud patterns (see Table 6). In fact, from the eight objects that satisfied the criteria for composite spectra candidates, six are known to have rotational modulations: 2M0624-45 (object 13), 2MUCD 10802 (object 19), 2M1039+32 (object 24), 2M1324+63 (object 27), 2M1219+31 (object 22), and 2M1632+19 (object 20). One is a confirmed binary, 2M1711+22 (object 8), and one has been reported as non-variable, 2M1515+48 (object 12).

These results suggest that Burgasser et al. (2006, 2010) and Bardalez Gagliuffi et al. (2014) spectral indices are biased toward L and T brown dwarfs that show photometric variability due to rotational modulations. Thus, these indices should also be useful to search for brown dwarfs candidates with heterogeneous cloud patterns in their atmospheres. In Table 8, we list all objects with L4 to T4 spectral types in our sample for which the method presented in this section are applicable. We specify which of them have reported rotational modulations in the literature, and we compare with those that have been found by the indices as composite spectra candidates.

We conclude that 21 out of the 32 objects listed in Table 7 have rotational modulations reported in the literature (see Table 8 for details); nonetheless, only nine are detected by the indices as candidates for composite spectra, with spectral types from L4 to T2 (spectral types from the literature). None of the low-gravity brown dwarfs found in Section 5 with reported rotational modulations have been detected by indices. In addition, the indices have detected three other candidates to have composite spectra, but they are not known to show rotational modulations.

7. Methane (1.2 μm) and Water (1.4 μm) Absorption Bands for Spectral Classification

The most prominent molecular absorption bands in the near-infrared spectra of brown dwarfs and substellar companions are H_2O , CO , and CH_4 . The absorption bands of the different molecules are controlled by the availability of C and O (Marley et al. 2010). Within the temperature range (approx. 1800 K to 600 K and below) of substellar objects in our sample—corresponding to spectral types from L4 to Y1—carbon appears mainly in the form of CO in L dwarfs and as CH_4 in T dwarfs (Marley & Robinson 2015). The equilibrium reaction that takes place is:



At higher temperature (L dwarfs), the left side of the reaction is favored; thus, there is an overabundance of CO , which implies an underabundance of H_2O . At lower temperatures, below the L/T transition, the right-hand side of the reaction is favored, leading to higher abundances of CH_4 and H_2O (Marley & Robinson 2015). The depth of some of these molecular bands in our *HST*/WFC3 spectra can serve to provide a robust spectral classification of substellar objects. In the *HST*/WFC3

Table 8
L4–T4 Dwarfs with Reported Rotational Modulations and Composite Atmosphere Candidates

Num.	Name	Variable?	Detected by Indexes	Confirmed As Candidate
1	CD-352722b	...	No	No
2	2MASS J17502484+0016151	Yes (1)	Yes	No
3	2MASS J03552337+1133437	...	No	No
4	2MASS J18212815+1414010	Yes (2)	No	No
5	2MASSW J1507476+162738	Yes (2)	Yes	No
6	2MASSI J0421072+630602	No (1)	No	No
7	2MASS J05395200+0059019	No (1)	No	No
8	2MASSI J1711457+223204	No, binary (1)	Yes	Yes
9	2MASS J00470038+6803543	Yes (3)	No	No
10	LP261-75B	Yes (4)	No	No
11	2MASS J01075242+0041563	Yes (5)	No	No
12	2MASSW J1515008+484742	No (1)	Yes	No
13	2MASS J06244595+4521548	Yes (1)	Yes	Yes
14	2MASSW J0801405+462850	No (1)	No	No
15	PSO J318.5+22	Yes (6)	No	No
16	2MASSW J2224438+015852	No (7)	No	No
17	Luh 16AB	Yes (8)	No	No
18	2MASSI J0825196+211552	No (1)	No	No
19	2MUCD 10802	No (1)	Yes	No
20	2MASS J16322911+1904407	Yes (1)	Yes	Yes
21	2MASSW J0310599+164816	Yes (1)	Yes	No
22	2MASS J12195156+3128497	Yes (1)	Yes	Yes
23	SDSS J075840.33+324723.4	Yes (13)	No	No
24	2MASS J10393137+3256263	Yes (1)	Yes	Yes
25	2MASS J09090085+6525275	No (1)	Yes	No
26	2MASS J21392676+0220226	Yes (9), (14)	No	No
27	2MASS J13243553+6358281	Yes (1), (14)	Yes	Yes
28	2MASS J16291840+0335371	Yes (13)	No	No
29	HN PEG B	Yes (10)	No	No
30	SIMP J013656.5+093347.3	Yes (11), (14)	No	No
31	GU PSC B	Yes (12)	No	No
32	2MASS J17503293+1759042	Yes (1)	No	No

References. (1) Buenzli et al. (2014); (2) Yang et al. (2015); (3) Lew et al. (2016); (4) Manjavacas et al. (2018); (5) D. Apai et al. 2018, preparation; (6) Biller et al. (2018); (7) Metchev et al. (2015); (8) Buenzli et al. (2015); (9) Radigan et al. (2012); (10) Zhou et al. (2018); (11) Artigau et al. (2009); (12) Naud et al. (2017); (13) Radigan et al. (2014); (14) Apai et al. (2017).

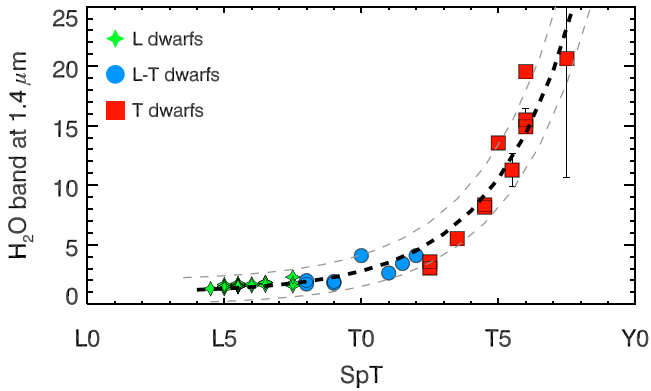


Figure 7. Evolution of the depth of the H₂O band at 1.4 μm with near-infrared spectral types calculated using Equation (4). The value of the depth of the H₂O band is dimensionless.

1.10–1.69 μm spectra of brown dwarfs and substellar companions, we are able to measure the depth of the CH₄ band at approximately 1.2 μm and the H₂O band at approximately 1.4 μm , and we can trace their change in depth with near-infrared spectral types (see Figures 7 and 8). We measured the

depths of the H₂O and CH₄ bands using Equation (1) from Allers & Liu (2013):

$$\text{index} = \left(\frac{\lambda_{\text{line}} - \lambda_{\text{cont1}}}{\lambda_{\text{cont2}} - \lambda_{\text{cont1}}} F_{\text{cont2}} + \frac{\lambda_{\text{cont2}} - \lambda_{\text{line}}}{\lambda_{\text{cont2}} - \lambda_{\text{cont1}}} F_{\text{cont1}} \right) / F_{\text{line}}. \quad (4)$$

In Table 9, we show the wavelengths at which the continuum, the center, and the width of the bands are defined. The minimum value of this index is 1, implying that there is no absorption feature. In addition, we derive an exponential function to relate the near-infrared spectral types and the depths of the CH₄, as well as the H₂O bands. To calculate the best-fit exponential function, we used the IDL function COMFIT.PRO, which fits an exponential equation of the form $y = c_0 * c_1^x + c_2$ using a gradient-expansion least-squares method (Marquardt 1963). The exponential function was preferred over polynomial functions because it provides a smaller reduced χ^2 . We did not include Y dwarfs in the fit, due to their lower quality data (see Table 1), nor hot Jupiters, as their atmospheres are, in general, physically different. To obtain the CH₄ index, we also discarded some companions (CD-352722 B, HN-Peg B, and GU PSC B)

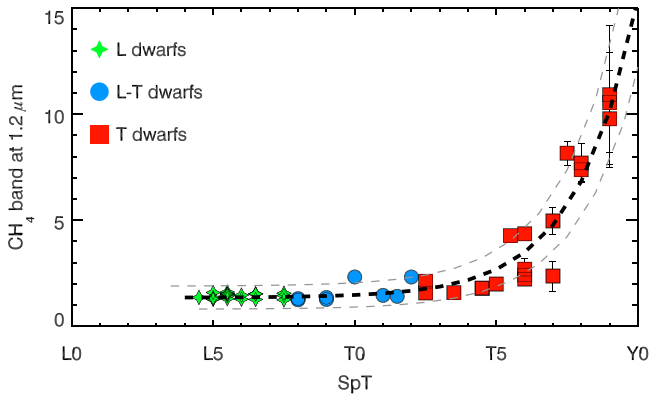


Figure 8. Evolution of the depth of the CH_4 band at $1.2 \mu\text{m}$ with near-infrared spectral types calculated using Equation (4). The value of the CH_4 band is dimensionless.

Table 9

Wavelength for the Continuum and Central Wavelengths in which the Depth of the CH_4 and H_2O Bands are Measured

Index	λ_{line}	λ_{cont1}	λ_{cont2}	Band Width
H_2O	1.40	1.31	1.47	0.08
CH_4	1.18	1.10	1.30	0.12

Note. Wavelength units are μm .

because they were outliers in the SpT versus CH_4 index plot, probably due to contamination of the star at the wavelength range in which the CH_4 index is measured. The best fits to exponential functions are displayed in Figures 7 and 8 with a dashed thick black line. The gray dashed lines in those figures represent the standard deviation of the data points with respect to the fitted function. The values of the coefficients for each best fit exponential functions are displayed in Table 10. In addition, in the former table, we also show the function that provides spectral types of brown dwarfs given the value of the H_2O and CH_4 bands. In Table 11, we present the typical dimensionless values for the H_2O and CH_4 bands calculated using the exponential functions indicated in Table 10. The depths of the H_2O and CH_4 bands can provide robust spectral classification for brown dwarfs with high-quality near-infrared spectra including the $1.4 \mu\text{m}$ water band. This is especially true for brown dwarfs with spectral types later than T2, for which the change of the bandwidth is more abrupt with spectral type.

8. Comparison of Brown Dwarfs' and Hot Jupiters' Photometry and Spectra

Color-magnitude diagrams have been traditionally used to directly compare the colors and absolute magnitudes of low-mass stars and brown dwarfs (Burgasser et al. 2008; Dupuy & Liu 2012; Faherty et al. 2012, and references therein), revealing that different parameters influence the atmospheres of these objects. Apart from effective temperatures, other secondary parameters that influence brown dwarfs colors include surface gravity, metallicity, dust sedimentation, and non-equilibrium chemistry. Brown dwarfs and hot Jupiters share similar effective temperatures and size ranges. Nevertheless, direct comparisons are usually challenging, as hot Jupiters orbit at

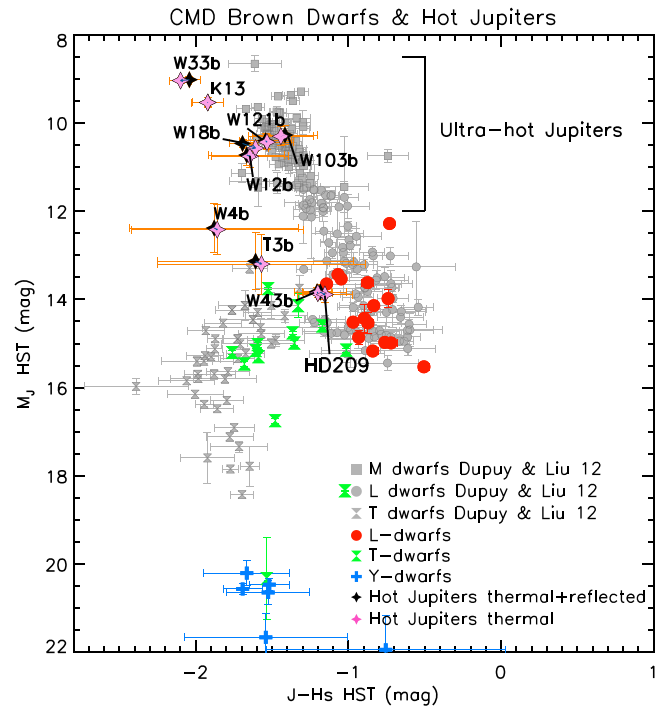


Figure 9. CMD diagram showing brown dwarfs and hot Jupiters together. Red dots represent L dwarfs, green hourglasses represent T dwarfs, and blue crosses represent Y dwarfs. Hot Jupiters are shown as black stars. After removing the contribution of their albedo (thermal flux), hot Jupiters are shown as pink stars.

close proximity to their host stars—and therefore, they are highly irradiated and difficult to observe directly.

In this section, we compare the hot Jupiters' *HST*/WFC3 near-infrared day-side emission photometry and spectra (see Table 2) to similar photometry and spectra of field and young brown dwarfs, to explore differences and similarities between these two classes of substellar objects (see Figure 9).

Before proceeding to the spectral comparison, we need to transform the relative flux density typically given for eclipse depth (ED) (a ratio between the flux densities of the planet and the host star, $F_{\lambda,\text{planet}}/F_{\lambda,\text{star}}$), to absolute (physical) flux density. If the flux of the planet is given in relative ED, we transform first those units to relative flux given in $F_{\text{planet}}/F_{\text{star}}$ by:

$$\frac{F_{\lambda,\text{planet}}}{F_{\lambda,\text{planet}} + F_{\lambda,\text{star}}} = \text{ED} \rightarrow \frac{F_{\lambda,\text{planet}}}{F_{\lambda,\text{star}}} = \frac{1}{1/\text{ED} - 1}. \quad (5)$$

Once the flux of the planet is given in $F_{\lambda,\text{planet}}/F_{\lambda,\text{star}}$, to transform to actual physical flux density units, we use a model spectrum for the temperature and surface gravity of the spectral type of each the parent stars given in Table 2. We used the BT-Settl atmospheric models (Allard et al. 2012), scaling the model absolute flux by $(R/d)^2$, where R is the radius of the star in m, and d is the distance of the system to Earth. The star radii were obtained from Table 5 from Pecaut & Mamajek (2013). We used trigonometric distances available either from the *Gaia* DR2 (Gaia Collaboration et al. 2018) or in the literature. Finally, we binned the stellar model spectra to match the corresponding *HST*/WFC3 spectra bins for each hot Jupiter, and obtained the physical flux density for each planet solving

Table 10
Exponential Functions Relating the Depth of the CH₄ Band at 1.2 μm and H₂O Band at 1.4 μm with Near-infrared Spectral Types

x	y	Exponential Fit			χ_{red}^2
		c_0	c_1	c_2	
NIR SpT	CH ₄	$(1.13 \pm 1.09) \times 10^{-3}$	1.60 ± 0.08	1.35 ± 0.20	1.32
NIR SpT	H ₂ O	$(6.51 \pm 1.90) \times 10^{-2}$	1.40 ± 0.03	$(9.71 \pm 2.57)10^{-1}$	1.31

Notes. The exponential function is defined as: $y = c_0 * c_1^x + c_2$. To obtain NIR spectral types from the value of the index: $x = \log_{c_1} \left(\frac{y - c_2}{c_0} \right)$.

Table 11

Typical Dimensionless Values for the H₂O and CH₄ Bands per Spectral Type Calculated Using the Corresponding Exponential Function in Table 10

SpT	Value CH ₄ Index	Value H ₂ O Index
L4	1.35 ± 0.54	1.21 ± 1.01
L5	1.36 ± 0.54	1.31 ± 1.01
L6	1.37 ± 0.54	1.45 ± 1.01
L7	1.38 ± 0.54	1.64 ± 1.01
L8	1.40 ± 0.54	1.90 ± 1.01
L9	1.43 ± 0.54	2.27 ± 1.01
T0	1.47 ± 0.54	2.79 ± 1.01
T1	1.55 ± 0.54	3.50 ± 1.01
T2	1.67 ± 0.54	4.50 ± 1.01
T3	1.87 ± 0.54	5.89 ± 1.01
T4	2.18 ± 0.54	7.84 ± 1.01
T5	2.68 ± 0.54	10.54 ± 1.01
T6	3.48 ± 0.54	14.32 ± 1.01
T7	4.77 ± 0.54	19.60 ± 1.01
T8	6.83 ± 0.54	26.95 ± 1.01
T9	10.13 ± 0.54	37.20 ± 1.01

Equation (5) as:

$$F_{\lambda, \text{planet}} = \frac{F_{\lambda, \text{star}}}{1/\text{ED} - 1}. \quad (6)$$

Once we transformed the units of hot Jupiter spectra to physical units ($F_{\lambda, \text{planet}}$ in $\text{erg s}^{-1} \text{cm}^{-2} \text{\AA}^{-1}$), we obtained *HST*/WFC3 photometric magnitudes in the *J* (1.10–1.35 μm) and *H_s*-band (1.50–1.69 μm) for each hot Jupiter and brown dwarf in our sample. The total flux in each band was calculated by integrating the flux densities in the relevant wavelength ranges. To obtain *J* and *H_s* *HST*/WFC3 magnitudes:

$$\text{STmag}_{J/H_s} = -2.5 \log F_{\lambda, \text{planet}} - \text{ZP}_{J/H_s}, \quad (7)$$

where $F_{\lambda, \text{planet}}$ is given in $\text{erg s}^{-1} \text{cm}^{-2} \text{\AA}^{-1}$, and ZP is the zeropoint in the *J* or *H_s*-band. We use the zero points for the F125W ($\text{ZP}_{\text{F125W}} = 25.3293$, in Vega magnitude) and the F160W filters ($\text{ZP}_{\text{F160W}} = 24.6949$, in Vega magnitude) that are centered at those bands.¹⁶

To compare the colors of highly irradiated hot Jupiters and isolated brown dwarfs, we plot a *J*–*H_s* *HST* color versus *M_J* *HST* magnitude in a CMD diagram with all brown dwarfs with available trigonometric parallax and all hot Jupiters in Figure 8. For comparison, we include M–Y dwarfs presented in Dupuy & Liu (2012) after transforming their 2MASS photometry to *HST* photometry using the polynomials presented in Appendix B. Gray squares represent M dwarfs, gray dots are L dwarfs, and gray hourglass symbols correspond to T dwarfs. In addition, we add the targets from our sample with trigonometric parallax: red dots are L dwarfs, green hourglass symbols are T dwarfs,

blue crosses are Y dwarfs, black stars are hot Jupiters, and pink stars are hot Jupiters after removing the contribution from the reflected light of the host star. The observed flux from the hot Jupiter is:

$$F_{\lambda, \text{planet}} = F_{\lambda, \text{thermal}} + F_{\lambda, \text{reflected}}, \quad (8)$$

where $F_{\lambda, \text{planet}}$ is the observed hot Jupiter spectra, $F_{\lambda, \text{thermal}}$ is the thermal flux from the planet, and $F_{\lambda, \text{reflected}}$ is the flux reflected from the star by the planet in the near-infrared, that depends on its albedo at those wavelengths.

$$F_{\lambda, \text{thermal}} = F_{\lambda, \text{planet}} - F_{\lambda, \text{reflected}}, \quad (9)$$

where

$$F_{\lambda, \text{reflected}} = A \times \frac{F_{\lambda, \text{star}}}{4\pi a_{\text{star-planet}}^2} \times 4\pi R_{\text{planet}}^2. \quad (10)$$

A is the geometrical albedo in the near-infrared. The geometrical albedo is wavelength-dependent and varies depending on multiple factors, including the composition of the planetary atmosphere, particle sizes in its atmosphere, surface gravity, etc. (Marley et al. 1999). As it is non-trivial to determine the wavelength dependency of hot Jupiter geometrical albedo, we assume a maximum near-infrared constant albedo of 0.1 for the estimation of the reflected flux from the star, as predicted by Marley et al. (1999). $F_{\lambda, \text{star}}$ is the flux density of the star given by the corresponding model spectra (Allard et al. 2012), scaled to the star’s distance from Earth. The scaling was done by multiplying the model spectrum by $(R_{\text{star}}/d_{\text{star-}\oplus})^2$, where R_{star} is the radius of the star (obtained from Pecaut & Mamajek 2013) and $d_{\text{star-}\oplus}$ is the distance between Earth and the star (based on the trigonometric parallaxes of the host stars, see references in Table 2). Here, $a_{\text{star-planet}}$ is the star–planet distance, available in the literature for all hot Jupiters (see Table 2). Finally, R_{planet} is the radius of each planet (Table 2).

As seen in Figure 8, the contribution of the albedo-assumed reflected light to the observed *HST*/WFC3 emission spectra is almost negligible, and it does not significantly change the colors and/or absolute magnitudes of the hot Jupiters considered in this study.

Ultra-hot Jupiters are a recently identified subgroup within hot Jupiters. The six brightest hot Jupiters in our sample belong to this category (WASP-33B, Kepler-13Ab, WASP-18b, WASP-121b, WASP-103b, and WASP-12b). Lothringer et al. (2018) and Parmentier et al. (2018) among others proposed that, under extreme irradiations, strong molecular dissociations and H[−] opacity will significantly reduce or even eliminate the molecular absorption bands in the dayside emission spectra of hot Jupiters. In our spectral library, these *ultra-hot Jupiters* all appear to lack the 1.4 μm water absorption band (Figure 10), while they have consistent *J* – *H* colors with the color sequence defined by M dwarfs (Figure 8). This agrees with the T_{eff} of 2500–3000 K estimated by Haynes et al. (2015), Beatty et al. (2017),

¹⁶ http://www.stsci.edu/hst/wfc3/ir_phot_zpt

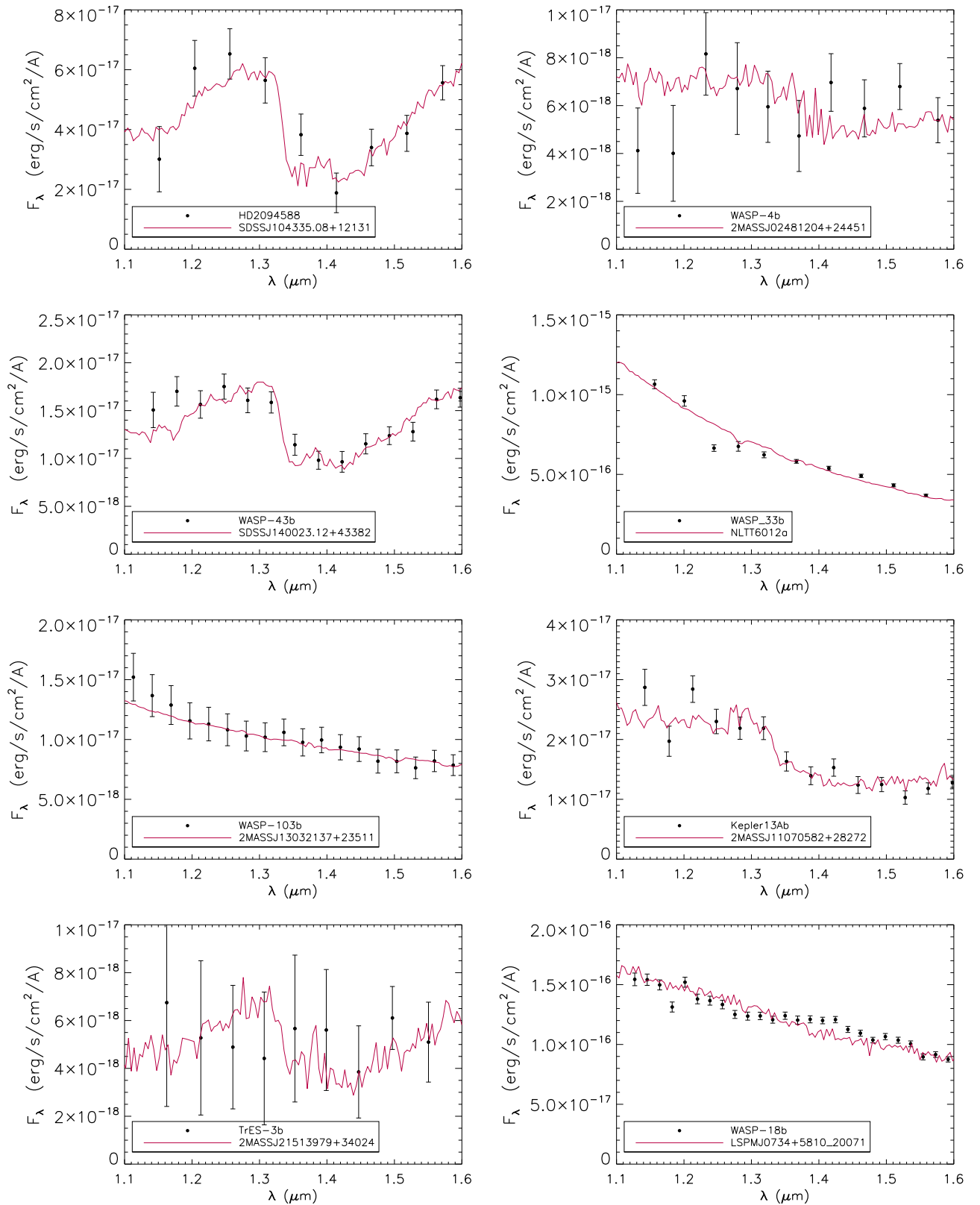


Figure 10. Best matches of hot Jupiters to brown dwarf spectra and M-dwarfs.

Sheppard et al. (2017), Evans et al. (2017), Cartier et al. (2017) and Stevenson et al. (2014a), respectively, for the ultra-hot Jupiters in our sample. WASP-4b and TrES-3b have M_J similar to those of early-type L dwarfs (Dupuy & Liu 2012), with similar T_{eff} of ~ 2000 K (Ranjan et al. 2014). Finally, HD 209458B and

WASP-43b have estimated T_{eff} of ~ 1500 – 1700 K (Stevenson et al. 2014b; Line et al. 2016), similar to those of mid-L dwarfs, and actually lie among other mid-L dwarfs in Figure 8.

Finally, we compared the *HST*/WFC3 hot Jupiter emission spectra compiled in this work to spectra collected in the SpeX

Spectral Library. We chose the best fits based on the value of their modified χ^2 (G), as obtained using Equation (1), as well as visual inspection. We found that only three of the ten hot Jupiters in our study had best matches to mid-L dwarfs: HD 209458B was matched to SDSS J104335.08+12131 (L7), WASP-43b was matched to SDSS J140023.12+43382 (L7), and TrES-3b was matched to 2MASS J21513979+34024 (L7 peculiar). The other seven hot Jupiters are best matched to M-dwarfs: WASP-33b, WASP-103b, and WASP-18b are best matched by M3-type stars (NLTT 6012a, 2MASSJ13032137+23511, and LSPMJ0734+5810, respectively). Kepler-13Ab is best matched by 2MASS J11070582+28272 (M7), which is consistent with the result of Beatty et al. (2017), who found a best match to an M8 brown dwarf. WASP-4b best matched to 2MASS J02481204+24451 (M8). Finally, we did not find a best match for WASP-12b or WASP-121b (see Figure 10).

These results are generally consistent with the positions of hot Jupiters within the CMD in Figure 8, as well as with the temperatures predicted for those objects by their respective authors. In addition, these results also agree with predictions made by the atmospheric models presented by Fortney et al. (2008), who suggested that there are two classes of hot Jupiter dayside atmospheres analogous to the M- and L dwarfs spectral types, which they called pM and pL , respectively. The pM class planets have hot stratospheres due to the high irradiation of their parent star ($T_{\text{eff}} > 2000$ K), with temperature inversion in their atmospheres and molecular bands in emission. The models predict that the temperature differences between their day- and nightsides are high due to radiative time constants at photospheric pressures that are shorter than advective time-scales. In contrast, the pL class planets are less irradiated by their parent star. The incident flux from the parent star is absorbed in the atmosphere and redistributed easily, as there is no thermal inversion in their photospheres. Thus, they have cooler daysides and warmer nightsides. Their spectra are dominated by H_2O in the near-infrared, and by Na and K absorptions in the optical.

Our results are consistent with, and expand upon, a previous study by Triaud (2014), who compared transiting planet dayside emission measured in two Spitzer/IRAC bands ([3.6] and [4.5] filters) to those of brown dwarfs in a CMD plot. This comparison suggested overall similarity, with a few possible outliers. The Spitzer color-magnitude comparison is particularly sensitive to the presence/absence of methane absorption. In a followup work, Triaud et al. (2014) extended their study to near-infrared continuum bands, and to a larger sample using photometric distances to compare their objects with brown dwarfs in a CMD plot. They found that, for a given luminosity, hot Jupiters' daysides show larger ranges of colors than brown dwarfs, especially with decreasing intrinsic luminosity. In contrast, our study suggests that brown dwarfs and hot Jupiters tend to be similar in the shorter-wavelength continuum emission (J and H bands) bands and that, for many hot Jupiters, brown dwarfs can provide surprisingly good spectral matches.

Fortney et al. (2008) used these atmospheric models to predict the classes of several hot Jupiters, in which TrES-3b and HD 209458B were included. They found that TrES-3b should belong to the pM class, as we consistently obtained. They also predicted HD 209458B to be in the transition zone between both classes, but as Line et al. (2016) also found, we

conclude that this hot Jupiter matches better to an L-dwarf spectrum, and thus to the pL class.

9. Summary and Conclusions

We present a very high-quality *HST*/WFC3 near-infrared spectral library of brown dwarfs (field and companions to stars), planetary-mass objects, and hot Jupiters, to enable quantitative comparative studies. In this paper, we provide an initial characterization and analysis of these *HST*/WFC3 near-infrared spectra:

1. In Section 3, we uniformly derive near-infrared spectral types for the brown dwarfs and the substellar companions to stars, using the SpeX Spectral Library templates for comparison. We conclude that their spectral types are mostly consistent with the spectral types provided in the literature within ± 1.5 subspectral types. The only exception is for low surface-gravity objects, for which the differences found are ± 3 spectral types. This is expected, as the SpeX Spectral Library templates are mostly composed of field gravity low-mass stars and brown dwarfs.
2. In Section 4, we plot an M_J versus $J - H$ CMD to compare our sample to other substellar objects, with the objective of identifying brown dwarfs with peculiar colors/brightness, including red or blue objects, low-surface gravity objects, binaries, etc. We find that objects 32 (2M1750+1759, known binary) and 34 (2M0559-34, overluminous), are overluminous in the CMD, suggesting that they are potential multiple systems.
3. In Section 5, we obtain the H -continuum and KI_J near-infrared spectral indices from Allers & Liu (2013) to search for potential L4 to L8 low-surface gravity substellar objects in our sample. We found two very low-gravity dwarfs: CD-352722B (object 1) and 2M0355+1133 (object 3). In addition, we found five intermediate surface-gravity objects: 2M0421-6306 (object 6), W0047 (object 9), 2M0107+0041 (object 11), PSO J318.5-22 (object 15), and 2M2224-0158 (object 16).
4. In Section 6, we apply the method from Burgasser et al. (2006, 2010) and Bardalez Gagliuffi et al. (2014) to search for candidates for composite spectra in our sample. Their spectral indices selected 13 composite spectra candidates, from which eight were selected from the F-statistic analysis described in Section 6. None of these eight objects are overluminous, as would be expected for binary or multiple brown dwarfs systems. In addition, we found that five of the eight selected objects have been reported in the literature as photometrically variable. Thus, this method might be useful to find potential variable late-L and early-T dwarfs. Nevertheless, we also found that not all objects in our sample with reported photometric variability have been detected by the Burgasser et al. (2006, 2010) and Bardalez Gagliuffi et al. (2014) method. The indices themselves detected 9 out of 19 variables and three no-variable objects in our sample, with spectral types between L4 and T2.
5. In Section 7, we measure the depths of the water band at $\sim 1.4 \mu\text{m}$ and the methane band at $\sim 1.2 \mu\text{m}$ for brown dwarfs and substellar companions to stars. We derive a relation between their near-infrared spectral types and the

depths of those bands, providing a tool for spectral classification of other substellar objects.

6. In Section 8, we compare the emission spectra of the dayside of hot Jupiters to the spectra of brown dwarfs and substellar companions to stars in our sample and low-mass stars and brown dwarfs from the SpeX spectral library. We found best matches to either L or M-dwarfs for eight out of the ten hot Jupiters of our sample. In addition, we plot a CMD using J and H_{short} *HST* bands for all our sample. The hottest hot Jupiters, WASP-33B, Kepler-13Ab, WASP-18b, WASP-121b, WASP-103b, and WASP-12b have M_J magnitudes similar to those of mid-M dwarfs (Dupuy & Liu 2012), which agrees with the T_{eff} of 2500–3000 K estimated by their respective authors. WASP-4b and TrES-3b have M_J similar to those of early L dwarfs (Dupuy & Liu 2012), with likewise similar T_{eff} of ~ 2000 K. Finally, HD 209458B and WASP-43b have estimated T_{eff} of ~ 1500 – 1700 K (Line et al. 2016; Stevenson et al. 2014b, respectively) similar to those of mid-L dwarfs, and actually lie among other mid-L dwarfs in the CMD diagram.

The *HST*/WFC3 near-infrared spectra presented in this work are available in machine-readable table files in a .tar.gz package. The spectra include wavelength, flux, and uncertainty in flux. The spectral library is also available at the High-level Science Products website at the MAST archive under the Cloud Atlas program’s page [10.17909/t9-asft-6k38](https://archive.stsci.edu/cloudatlas/).

We thank our anonymous referee for useful comments that helped to improve our paper. This work is based on observations made with the NASA/ESA *Hubble Space Telescope*, obtained at the Space Telescope Institute, which is operated by AURA, Inc., under NASA contract NAS 5-26555, under GO-13241, GO-14241, GO-12550, GO-13176, GO-12550, GO-13299, GO-13280, GO-13281, GO-12314, GO-14051, GO-12217, GO-13178, GO-12970, GO-12230, GO-13467, GO-12495, GO-14050, GO-13467, GO-12181, GO-13308, and GO-14767. This publication makes use of data products from the Two Micron All Sky Survey, which is a joint project of the University of Massachusetts and the Infrared Processing and Analysis Center/California Institute of Technology, funded by the National Aeronautics and Space Administration and the National Science Foundation. This work makes use of the SpeX Prism Spectral Library. This work has also made use of data from the European Space Agency (ESA) mission *Gaia* (<https://www.cosmos.esa.int/gaia>), processed by the *Gaia* Data Processing and Analysis Consortium (DPAC, <https://www.cosmos.esa.int/web/gaia/dpac/consortium>). Funding for the DPAC has been provided by national institutions, in particular, the institutions participating in the *Gaia* Multilateral Agreement. We have made use of the Matplotlib Python library (Hunter 2007).

Appendix A Data Set Description and Data Reduction

In the following, we summarize the key steps and references for the different data reductions performed on the spectra compiled in this work.

A.1. Brown Dwarf and Low-mass Companion Spectra

A.1.1. Time-resolved Spectra

We present the data sets with time-resolved spectroscopy taken for several of the brown dwarfs compiled in this work.

The Apai et al. (2013) data set consists of the first two brown dwarfs (SIMP J013656+093347 and 2MASS J21392676+0220226) observed in time-resolved observations and obtained in the GO-12314 program (PI Apai). Each objects was observed in six consecutive *HST* orbits. Apai et al. (2013) provides a detailed summary of the reduction procedure. In this spectral library, we present the median of the time-resolved spectra for each object.

The Buenzli et al. (2012) study presents near-infrared, time-resolved, six orbit-long spectroscopy of a single target (2M2228, object 37) that was reduced with a method identical to that in Apai et al. (2013). These data were also taken in program GO-12314 (PI: Apai), and the target was also a known variable brown dwarf. The observations showed spectral variability with pressure-dependent phase shifts Buenzli et al. (2012). We took the median of the time-resolved spectra for our library.

The Buenzli et al. (2014) sample consists of 22 brown dwarfs with spectral types between L5 and T6. These data were collected in an *HST* SNAP program (PO 12550, PI Apai). Basic reduction followed the same steps as for the previous programs. The ramp effect was corrected using an analytical function fitted to the flux of a nonvariable star as in Apai et al. (2013), in addition to removing the first 180 s of each time series where the scatter in the ramp effect is substantial.

The Buenzli et al. (2015) study presented spatially and temporally resolved spectroscopy for the Luhman 16 A and B binary brown dwarf components. Reduction followed the steps described in Apai et al. (2013) and Buenzli et al. (2014). We present the combined Luhman 16 A and B spectra in this paper.

The time-domain programs described above focused on relative variations and did not correct for wavelength-dependent aperture losses, which is not relevant in the related studies. However, these corrections are necessary for our purposes. We performed a uniform aperture correction on all sources from the above studies to correct for flux loss due to the finite width of the spectral extraction windows. We corrected for the missing flux per wavelength on the basis of measured wavelength-dependent flux losses, performing a bilinear interpolation in wavelength and aperture width of the values of the aperture corrections tabulated in Table 6 from Hartig (2009).

Within the *Cloud Atlas HST* treasury program (*HST* GO 14241), time-resolved spectroscopy observations for eight L4 to T7 high- and low-surface gravity brown dwarfs were obtained. The data were collected between 2015 September and 2018 September. The *Cloud Atlas* program uses time-resolved spectroscopy to probe the spatial distribution and properties of condensate clouds. A publication in preparation (D. Apai et al. 2018, in preparation) will provide an overview of the program and its key results from the time-resolved spectroscopy. Results for three objects have already been published (WISE0047: Lew et al. 2016; LP261-75B: Manjavacas et al. 2018; HN Peg B: Zhou et al. 2018), while other papers are in preparation (S0107: D. Apai et al. 2018, in preparation). Here, we present the spectral results based on time-averaged spectra for all objects. We performed the data reduction using methods very similar to those described above for previous studies (Buenzli et al. 2012,

2014, 2015; Apai et al. 2013, and references therein). An important difference, however, is the use of a significantly improved WFC3 ramp correction method. Zhou et al. (2017) identified charge trapping and delayed release as the cause of the “ramp effect,” and they developed a solid-state physics-based model capable of reliably correcting this effect in a wide variety of WFC3 data. Most of the *Cloud Atlas* data sets published use the ramp effect correction by Zhou et al. (2017). The uncertainty level for our spectra after the data reduction is 0.1–0.3% per spectral bin, measured using the reduced individual spectra. These uncertainties are due to photon noise, errors in the sky subtraction, and the readout noise. Finally, we performed aperture corrections following the same procedure as for the other spectra mentioned previously in this section.

Within the *HST* GO 13299 and 14051 (P.I. Radigan), time-resolved near-infrared spectra observations were obtained with *HST*/WFC3 to study the rotational modulations of two unusually blue L dwarfs. The objective of this project was to create spectrally and spatially resolved maps of these objects. These objects are SDSS J075840.33+324723.4 (object 23), and 2MASS J16291840+0335371 (object 28). SDSS J075840.33+324723.4 was observed during five consecutive orbits, and 2MASS J16291840+0335371 was observed during four consecutive orbits. The data reduction was performed using a procedure to that used for the *Cloud Atlas* treasury program data. In this paper, we present the median combined spectra of all the time-resolved near-infrared spectra taken during the consecutive orbits in which these objects were observed. The uncertainty level for these spectra after median-combining all time-resolved spectra is $\sim 0.03\%$ at $1.25 \mu\text{m}$. These uncertainties are due to photon noise, errors in the sky subtraction, and the readout noise.

Finally, Biller et al. (2018) present time-resolved spectroscopy of the red L7 dwarf, PSO 318-22. They differ from the previous studies in that the ramp correction was corrected using four background stars in the field of view (2–3 times brighter than the target). They median-combined and normalized the while light curves of the background stars to produce a calibration curve. They then divided the target’s light curve by the calibration curve to eliminate the ramp effect and other systematics, following an approach similar to that used by previous ground studies (Radigan 2014; Biller et al. 2015).

A.1.2. Single Spectra

S Ori 70 and S Ori 73 (Peña Ramírez et al. 2015) are $T7 \pm 0.5$ and $T4.5 \pm 0.5$ dwarfs, respectively. S Ori 70 and S Ori 73 were observed with *HST*/WFC3 (PI Lucas, *HST*-GO-12217). Details on the data reduction can be found in Peña Ramírez et al. (2015).

In addition, we include 22 T8 to Y2 brown dwarf spectra presented and analyzed in Schneider et al. (2015). The observations were carried out within the P.I. Kirkpatrick programs 12330 and 13178, and P.I. Cushing programs *HST*-GO-12544 and *HST*-GO-12970. Because G141, with which the observations were performed, is a slitless grism, the source spectra are sometimes contaminated by photons from nearby sources. To address this problem, Schneider et al. (2015) developed a source extraction routine to define source apertures and background regions on the individual images. After the best aperture is defined, aperture corrections and flux calibrations are performed following Kuntzschner et al. (2011). For objects with multiple visits, the images have been median-combined

to produce a final spectroscopic image. Finally, spectra are extracted as indicated above. The published spectra are time-averaged spectra.

A.2. Hot Jupiter Emission Spectra

In this section, we summarize the different reduction methods performed by the respective authors in which hot Jupiters’ emission spectra were published.

A.2.1. WASP-18b

The emission spectrum of WASP-18b was presented in Sheppard et al. (2017). Observations of three individual eclipse events were obtained during three epochs as part of the program GO 13467. At a fourth epoch, observations were obtained with two eclipses within an orbital phase curve. Grism observations were taken in spatial scan mode with forward-reverse cadence (Dressel 2019). Further details regarding the data reduction are found in Sheppard et al. (2017). Finally, a forward and a reverse scan light curve were obtained and analyzed separately. To correct non-astrophysical effects, the systematic trends were removed using parametric marginalization (Wakeford et al. 2016), and then further detrending was performed by the subtraction of scaled band-integrated residuals from wavelength bins (Haynes et al. 2015). The wavelength bins of the spectrum are given in Table 1 of Sheppard et al. (2017).

A.2.2. WASP-33b

The emission spectrum of WASP-33b was first published by Haynes et al. (2015). WASP-33b is orbiting a δ -Scuti star (Herrero et al. 2011) and its modulations were modeled with sine functions. To produce the 2D spectral frames from the files provided by the standard pipeline, a top hat mask was applied in the spatial direction of each read with a width of 20 pixels (Herrero et al. 2011). Subsequent reads were then subtracted and added to differenced frames to create one scanned image (Deming et al. 2013). To correct bad pixels, the method of Mandell et al. (2013) was used within the combined spectral frames, and the images were combined into 1D spectra. To perform the wavelength and flatfield wavelength-dependent calibrations, the coefficients from Wilkins et al. (2014) were used.

A.2.3. WASP-12b

The emission spectrum of WASP-12b was published in Stevenson et al. (2014a). The observations of WASP-12b were taken in five consecutive orbits in staring mode. Further details regarding the observations can be found in Swain et al. (2013). Data were reduced using the standard *HST* pipeline as explained in detail in Stevenson et al. (2014a).

To trace the first-order spectra, the direct image was located using a two-dimensional Gaussian, and then Table 1 of Kuntzschner et al. (2009) was used to provide a direct-to-dispersed image offset. The wavelength calibration is performed using the coefficients provided in Table 5 from Kuntzschner et al. (2009). The flat field was modeled using the standard calibration flat files. The spectral extraction was performed within a box of 150×150 pixels centered on the spectrum. The spectral extraction was performed along 40 pixels in the spatial direction, and the remaining pixels in the

Table 12
Log of the Sample of L, L-T, T, and Y Dwarfs with *HST*/WFC3 Spectroscopy

Num.	Name	Obs. Dates	Num. Orbits \times Visits	T_{exp} Single expo. (s)	Num. Single Expo./Orbit
1	CD-352722b	2015 Sep 7	2 \times 1	29.6	98
2	2MASS J17502484-0016151	2012 Jun 15	1 \times 1	22.6	64
3	2MASS J03552337+1133437	2015 Oct 6	2 \times 1	89.6	46
4	2MASS J18212815+1414010	2013 Jun 9 and Jun 27	3 \times 2	112.0	19
5	2MASSW J1507476-162738	2013 Apr 30 and May 12	4 \times 2	67.3	30
6	2MASSI J0421072-630602	2012 Mar 20	1 \times 1	112.0	19
7	2MASS J05395200-0059019	2012 Mar 1	1 \times 1	45.0	37
8	2MASSI J1711457+223204	2012 Aug 1	1 \times 1	223.7	9
9	2MASS J00470038+6803543	2016 Jun 6/07	6 \times 1	201.3	65
10	LP261-75B	2016 Dec 20	6 \times 1	201.4	66
11	2MASS J01075242+0041563	2017 Jan 2	6 \times 1	201.4	22
12	2MASSW J1515008+484742	2012 Feb 25	1 \times 1	45.0	36
13	2MASS J06244595-4521548	2012 May 8	1 \times 1	45.0	38
14	2MASSW J0801405+462850	2011 Nov 10	1 \times 1	223.7	11
15	PSO J318.5-22	2016 Sep 8	5 \times 1	278.0	9
16	2MASSW J2224438-015852	2015 Sep 9	2 \times 1	89.6	26
17	Luh 16AB	2013 Nov 8	5 \times 1	76.2	100
18	2MASSI J0825196+211552	2012 May 9	1 \times 1	112.0	21
19	2MUCD 10802	2011 Dec 9	1 \times 1	45.0	40
20	2MASS J16322911+1904407	2012 Aug 11	1 \times 1	223.7	9
21	2MASSW J0310599+164816	2012 Aug 25	1 \times 1	223.0	10
22	2MASS J12195156+3128497	2012 Jun 18	1 \times 1	223.7	9
23	SDSS J075840.33+324723.4	2014 Apr 12	5 \times 1	112.0	22
24	2MASS J10393137+3256263	2012 May 8	1 \times 1	223.7	11
25	2MASS J09090085+6525275	2012 Aug 21	1 \times 1	223.7	10
26	2MASS J21392676+0220226	2010 Oct 21	6 \times 1	22.3	11
27	2MASS J13243553+6358281	2012 Feb 25	1 \times 1	112.0	21
28	2MASS J16291840+0335371	2015 June 6	4 \times 1	112.0	21
29	HNPEGB	2017 May 16	6 \times 1	201.4	65
30	SIMP J013656.5+093347.3	2013 Sep 28 and Oct 7	4 \times 2	112.0	19
31	GUPSCB	2018 Jan 8	6 \times 1	201.4	43
32	2MASS J17503293+1759042	2012 Oct 5	1 \times 1	223.7	10
33	2MASS J00001354+2554180	2012 Sep 13	1 \times 1	45.0	40
34	2MASS J05591914-1404488	2011 Oct 16	1 \times 1	22.6	62
35	2MASSI J2339101+135230	2012 Aug 21	1 \times 1	223.7	11
36	2MASS J11101001+0116130	2016 Feb 10	2 \times 1	201.4	21
37	2MASS J22282889-4310262	2013 Jul 20 and 27	4 \times 2	201.3	39
38	2MASS J08173001-6155158	2011 Oct 9	1 \times 1	22.6	67
39	S Ori J053814.5-024512	2010 Sep 5	1 \times 1	602.7	4
40	2MASSI J0243137-245329	2011 Dec 31	1 \times 1	112.0	19
41	2MASS J16241436+0029158	2012 Jul 13	1 \times 1	112.0	17
42	CFBDSIR2149-0403	2015 Sep 9 and Nov 18	4 \times 2	290.7	16
43	S Ori J053814.5-024512	2010 Oct 6	1 \times 1	602.7	4
44	ROSS458C	2018 Jan 5 and 6	7 \times 1	201.4	21
45	WISEA J032504.52504403.0	2013 Aug 4	1 \times 1	403.0	4
46	WISEA J033515.07+431044.7	2013 Aug 30	1 \times 1	453.0	4
47	WISEA J040443.50642030.0	2013 Apr 9	1 \times 1	453.0	4
48	WISEA J221216.27693121.6	2013 Sep 11	1 \times 1	453.0	4
49	WISEA J094306.00+360723.3	2013 Feb 20	1 \times 1	503.0	4
50	WISEA J154214.00+223005.2	2012 Mar 4	1 \times 1	503.0	4
51	WISEA J035934.07540154.8	2011 Aug 10	1 \times 1	553.0	4
52	WISEA J041022.75+150247.9	2012 Sep 1	1 \times 1	503.0	4
53	WISEA J073444.03715743.8	2013 May 20	1 \times 1	453.0	4
54	WISEA J120604.25+840110.5	2013 Jul 15	1 \times 1	453.0	4
55	WISE J154151.65225024.9	2013 May 9	1 \times 1	453.0	4
56	WISEA J173835.52+273258.8	2011 May 12	1 \times 1	503.0	4
57	WISEA J205628.88+145953.6	2011 Sep 4	1 \times 1	503.0	4
58	WISEA J222055.34362817.5	2013 Jun 20	1 \times 1	1103.0	4
59	WISEA J220905.75+271143.6	2012 Sep 15	1 \times 1	503.0	4
60	WISEA J082507.37+280548.2	2014 Jan 17	1 \times 1	2406.0	3
61	WISEA J140518.32+553421.3	2011 Mar 14	1 \times 1	553.0	4
62	WISEA J163940.84684739.4	2013 Oct 29	1 \times 1	602.9	4
63	WISEA J053516.87750024.6	2011 Sep 27	1 \times 2	553.0	4
63	WISEA J053516.87750024.6	2012 Sep 17	1 \times 2	553.0	4

Table 12
(Continued)

Num.	Name	Obs. Dates	Num. Orbits \times Visits	T_{exp} Single expo. (s)	Num. Single Expo./Orbit
63	WISEA J053516.87750024.6	2013 Sep 27	1 \times 1	1269.0	6
64	WISEA J035000.31565830.5	2011 Aug 13	1 \times 1	553.0	4
65	WISEA J064723.24623235.4	2013 May 13 and 2013 Dec 29	1 \times 2	1203.0	6
66	WISEA J235402.79+024014.1	2013 Sep 22	1 \times 1	806.0	4
67	WASP-18b	2014 Apr–Jun and Aug	6 \times 4	73.74	8?
68	WASP-33b	2012 Nov 25 and 2013 Jan 14	5 \times 2	51.7	119
69	WASP-12b	2011 Apr 12	5 \times 1	7.35	188
70	WASP-121b	2016 Nov 10	5 \times 2	103	16
71	WASP-43b	2013 Nov 9 and Dec 5	14 \times 2	103.129	19
72	WASP-103b	2015 Jun 17 and 17	5 \times 2	81.089	12
73	TrES-3b	2011 March 02	4 \times 1	36.02	219
74	Kepler-13Ab	2014 Apr 28 and Oct 13	5 \times 2	7.6	101
75	HD 209458B	2014 Sep–Dec	5 \times 5	14.971	43
76	WASP-4b	2010 Nov 25	5 \times 1	36.02	268

box were used for the background subtraction, generating 11 light curves.

A.2.4. WASP-121b

The emission spectrum of WASP-121b was first presented in Evans et al. (2017). Data reduction was performed using the *HST*/WFC3 standard pipeline, the details of which are explained in Evans et al. (2017). The target flux was extracted by taking the difference between successive nondestructive reads. The background was measured as a median count of a box of 110 columns along the dispersion axis and 20 rows along the cross-dispersion axis. To remove flux contributions from nearby stars and cosmic-ray hits, all pixels above and below 35 pixels from the center of the spectrum along the cross-dispersion axis were set to zero. Finally, all frames were added together. The spectrum was then extracted by summing the flux within a rectangular aperture across the dispersion axis with apertures from 100 to 200 pixels. The data taken during the first *HST* orbit were discarded due to a strong ramp effect, along with the first exposure of the remaining *HST* orbits.

A.2.5. WASP-43b

The emission spectrum of WASP-43b was first presented in Stevenson et al. (2014b). The observations were performed during 13–14 *HST* orbits on each primary transit or secondary eclipse visit, each of them consisting of four orbits. Due to the ramp effect, the first orbit of each visit was removed from the analysis. For the rest, the ramp was fitted with an exponential ramp model. Further details regarding the data reduction can be found in Stevenson et al. (2014b).

A.2.6. WASP-103b

The emission spectrum of WASP-103b was first presented in Cartier et al. (2017). WASP-103b was observed with ten *HST* orbits in two visits. The first orbit of both visits was discarded.

To remove the background, images were created using sequential pairs of up-the-ramp readouts within each exposure. For those subframes, a conservative mask was used to determine the background region and measure the sky background level, assuming that is spatially flat and uniform due to the short exposure times. This background was subtracted from all subframes. In addition, a smaller mask was defined (Deming et al. 2013; Knutson et al. 2014) and all pixels outside of the

mask were zeroed. This helps to reduce noise and exclude cosmic rays (CRs) in the background area when later combining all subframes to determine the flux for each exposure. Special flat fields were created for the data reduction using the determined centroids in the spectral direction (X) and scan direction (Y) direct image frame, assuming that every column has the same wavelength (Cartier et al. 2017). Finally, to remove additional cosmic rays and bad pixels, a moving median filter was applied. The final extracted spectrum was binned to 22 wavelength channels.

Instrumental effects and systematics due to the ramp correction were removed using Gaussian Processes (GP) regression (Rasmussen & Williams 2006), which does not need to prespecify a parametric model. GP regression was used to find the best-fit light curve eclipse model (Cartier et al. 2017).

A.2.7. TrES-3b and WASP-4b

The emission spectra of TrES-3b and WASP-4b were first presented in Ranjan et al. (2014). The observations were carried out during four consecutive orbits during the eclipse of TrES-3b, and five consecutive orbits during the eclipse of WASP-4b. The first orbit of each observation was discarded to avoid the most prominent ramp effect systematics.

The details of the data reduction can be found in Ranjan et al. (2014). The background subtraction was performed by choosing a fixed area on the detector and matching the wavelength range of the spectrum free of object flux in the individual 2D images. These background columns are scaled to match the spectral extraction aperture. Finally, the extracted spectra were binned in wavelength to enhance the signal-to-noise per resolution element (see Ranjan et al. (2014) for the bin's wavelength range for each object).

A.2.8. Kepler-13Ab

The emission spectra of Kepler-13Ab were first presented in Beatty et al. (2017). The Kepler-13Ab system is composed of three stars: the planet host, Kepler-13A, and the unresolved binary Kepler-13BC, with the two components separated by 1''15 (Shporer et al. 2014).

The observations were carried out during two visits that were composed of a total of five *HST* orbits. The planet host star is in a close binary system. The data reduction includes primary subtraction. All details of the data reduction can be found in

Beatty et al. (2017). The cosmic-ray hits were removed separately in an area around the stellar spectra, and the area dominated by the sky background. Finally, the background was subtracted from each exposure by defining two background regions across the bottom and top of each of these images.

To perform a spectral extraction of Kepler-13Ab, the contribution of Kepler-13BC needs to be subtracted first. Using the WAYNE simulator (Varley et al. 2017), the artificial 2D spectra of Kepler-13BC were created and subtracted to create an undiluted 2D spectrum of Kepler-13A. Finally, to perform the light-curve extraction, the spectral trace of Kepler-13A was fitted with a Gaussian profile along the detector columns. The columns along the detector were then summed using an extraction aperture with a half width of 4.5 pixels, to generate a 1D spectrum of Kepler-13A.

The wavelength calibration was done using the direct image taken at the beginning of each of the visits. The X and Y location of both Kepler-13A and Kepler-13BC were determined on the detector subarray, and then Kuntschner et al. (2009) wavelength calibration method was implemented to calculate a wavelength solution for each star. The Paschen- β line visible at $1.282 \mu\text{m}$ was used to verify the accuracy of the wavelength calibration.

A.2.9. HD 209458B

The emission spectrum of HD 209458B was first presented in Line et al. (2016). HD 209458b was observed as part of the GO 13467 *HST* treasury program. It was observed during a

secondary eclipse over five visits, each with five *HST* orbits. The first orbit of each visit was excluded from the analysis to minimize the impact of the ramp effect on the data set. A direct image was taken at the beginning of each orbit to aid the wavelength calibration.

All details about the data reduction can be found in Line et al. (2016). To extract the 1D spectra, an optimal extraction was used (Horne 1986) with an extraction window of 110 pixel rows centered on the spectra and flanked by additional 110 pixels rows for background extraction. The spectra of all frames were combined. Finally, the combined spectra were divided into 10 spectroscopic bins.

Appendix B

Transformation from 2MASS to *HST* Magnitudes

We derive empirical relations to transform L and T brown dwarf magnitudes from the 2MASS to the *HST* photometric system. To obtain the *HST*/WFC3 near-infrared magnitudes, we follow the same procedure as in Section 8, Equation (7). In Figure 11, we show the relation between the *J*- and *H*-band 2MASS magnitudes, and the *J*- and *H_s*-bands in the *HST* photometric system. We do not include the T9–T9.5 dwarfs with high photometric uncertainties. Finally, we calculate a linear relationship between both photometric systems for the *J*- and the *H*-band independently. The coefficients for both relations are presented in Table 13.

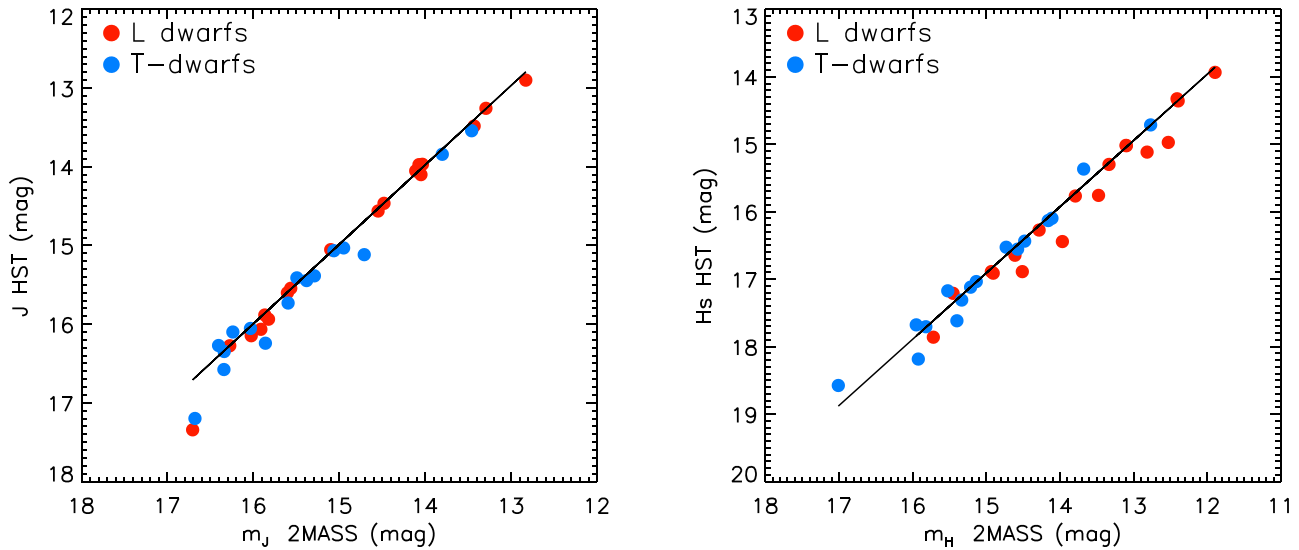


Figure 11. Relation between *J* and *H* 2MASS magnitudes, and *J* and *H_s* *HST* magnitudes for L and T dwarfs. L dwarfs are shown as red points, and T dwarfs are shown as blue points. Photometric uncertainties are smaller than the symbols.

Table 13

Linear Functions Relating the *J*- and *H*-band 2MASS Magnitudes and the *J* and *H_s* Respectively for L and T Brown Dwarfs

<i>x</i>	<i>y</i>	Linear fit	
		c_0	c_1
<i>J</i> 2MASS	<i>J</i> <i>HST</i>	-0.15535 ± 0.00254	1.00938 ± 0.00017
<i>H</i> 2MASS	<i>H_s</i> <i>HST</i>	2.17362 ± 0.00206	0.98229 ± 0.00014

Note. The linear function is defined as: $y = c_0 + c_1x$.

Table 14
Spectral Indices to Select L Plus T Brown Dwarf Binary Candidates

Index	Numerator Range ^a	Denominator Range ^a	Feature	Reference
H ₂ O-J	1.140–1.165	1.260–1.285	1.150 μm H ₂ O	1
CH ₄ -J	1.315–1.340	1.260–1.285	1.320 μm CH ₄	1
H ₂ O-H	1.480–1.520	1.560–1.600	1.400 μm H ₂ O	1
CH ₄ -H	1.635–1.675	1.560–1.600	1.650 μm CH ₄	1
H-dip	1.610–1.640	1.560–1.590+1.660–1.690 ^b	1.650 μm CH ₄	2
J-slope	1.27–1.30	1.30–1.33	1.28 μm flux peak shape	4
J-curve	1.04–1.07+1.26–1.29 ^c	1.14–1.17	Curvature across J-band	4
H-bump	1.54–1.57	1.66–1.69	Slope across H-band peak	4
Derived NIR SpT			Near-infrared spectral type ^d	1

Notes.

^a Wavelength range (in nm) over which flux density is integrated.

^b Denominator is the sum of the flux in the two wavelength ranges.

^c Numerator is the sum of the two ranges.

^d Near-infrared spectral type derived using comparison to SpeX spectra.

References. (1) Burgasser et al. (2006), (2) Burgasser et al. (2010), (3) Burgasser et al. (2002), (4) Bardalez Gagliuffi et al. (2014).

Table 15
Index Criteria for the Selection of Potential Brown Dwarf Binary Systems

Abcissa	Ordinate	Inflection Points
H ₂ O-H	H-dip	(0.5, 0.49), (0.875, 0.49)
Spex SpT	H ₂ O-J/H ₂ O-H	(L8.5, 0.925), (T1.5, 0.925), (T3, 0.85)

Table 16
Delimiters for Selection Regions of Potential Brown Dwarf Binary Systems

Abcissa	Ordinate	Limits
SpT	CH ₄ -H	Best fit curve: $y = -4.3x10^{-4}x^2 + 0.0253x + 0.7178$
H ₂ O-J	CH ₄ -H	Intersection of: $-0.08x + 1.09$ and $x = 0.90$
H ₂ O-J	H-bump	Intersection of: $y = 0.16x + 0.806$ and $x = 0.90$
CH ₄ -J	CH ₄ -H	Intersection of: $y = -0.56x + 1.41$ and $y = 1.04$
CH ₄ -J	H-bump	Intersection of: $y = 1.00x + 0.24$, $x = 0.74$ and $y = 0.91$
CH ₄ -H	J-slope	Intersection of: $y = 1.250x - 0.207$, $x = 1.03$ and $y = 1.03$
CH ₄ -H	J-curve	Best fit curve: $y = 1.245x^2 - 1.565x + 2.224$
CH ₄ -H	H-bump	Best fit curve: $y = 1.36x^2 - 4.26x + 3.89$
J-slope	H-dip	Intersection of $y = 0.20x + 0.27$ and $x = 1.03$
J-slope	H-bump	Intersection of: $y = -2.75x + 3.84$ and $y = 0.91$
J-curve	H-bump	Best fit curve: $y = 0.269x^2 - 1.326x + 2.479$

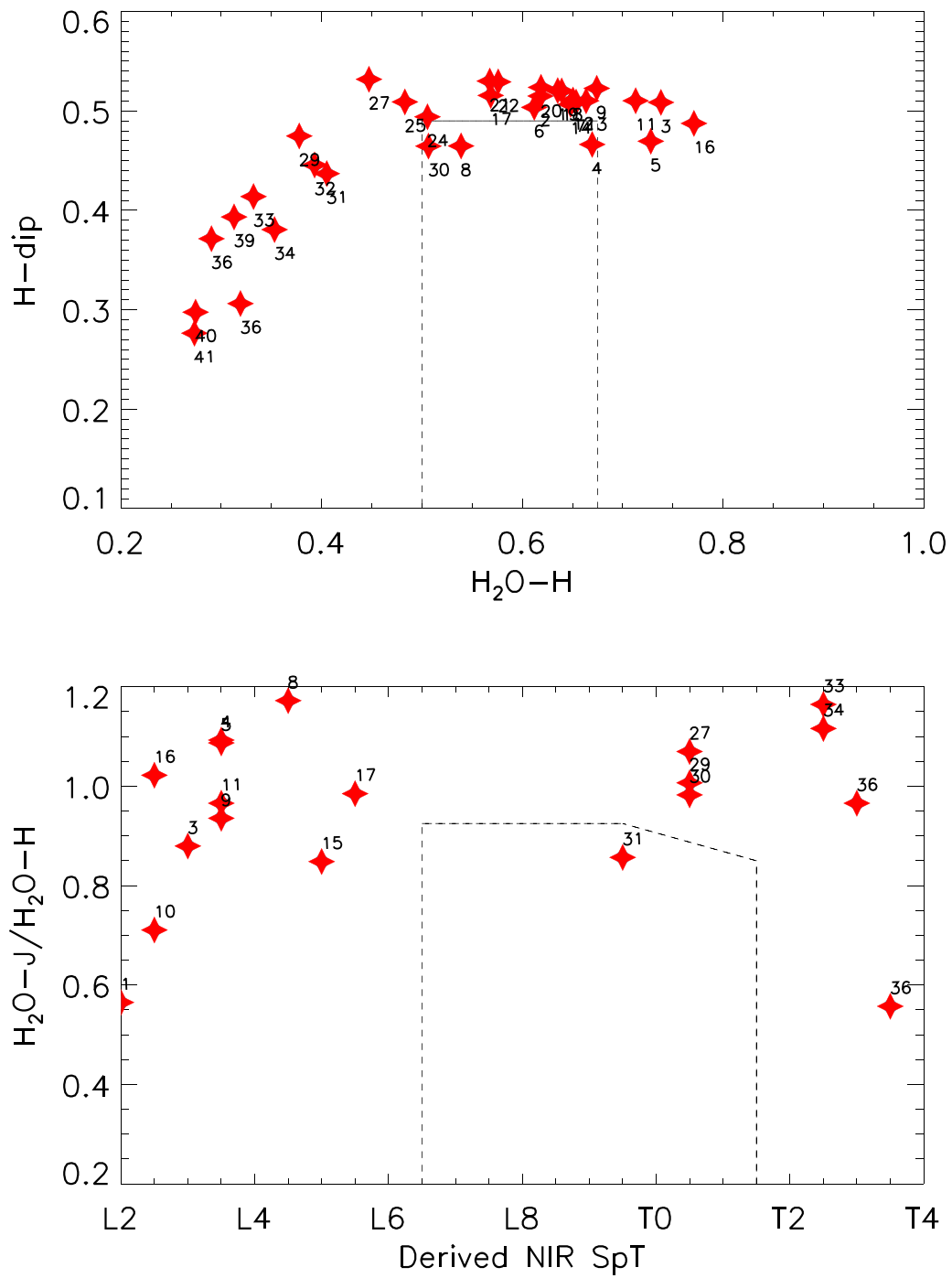


Figure 12. Spectral index selection. Numbers correspond to our objects. The boxes shown with dashed lines mark the areas where the selection criteria of Tables 15 and 16 are valid.

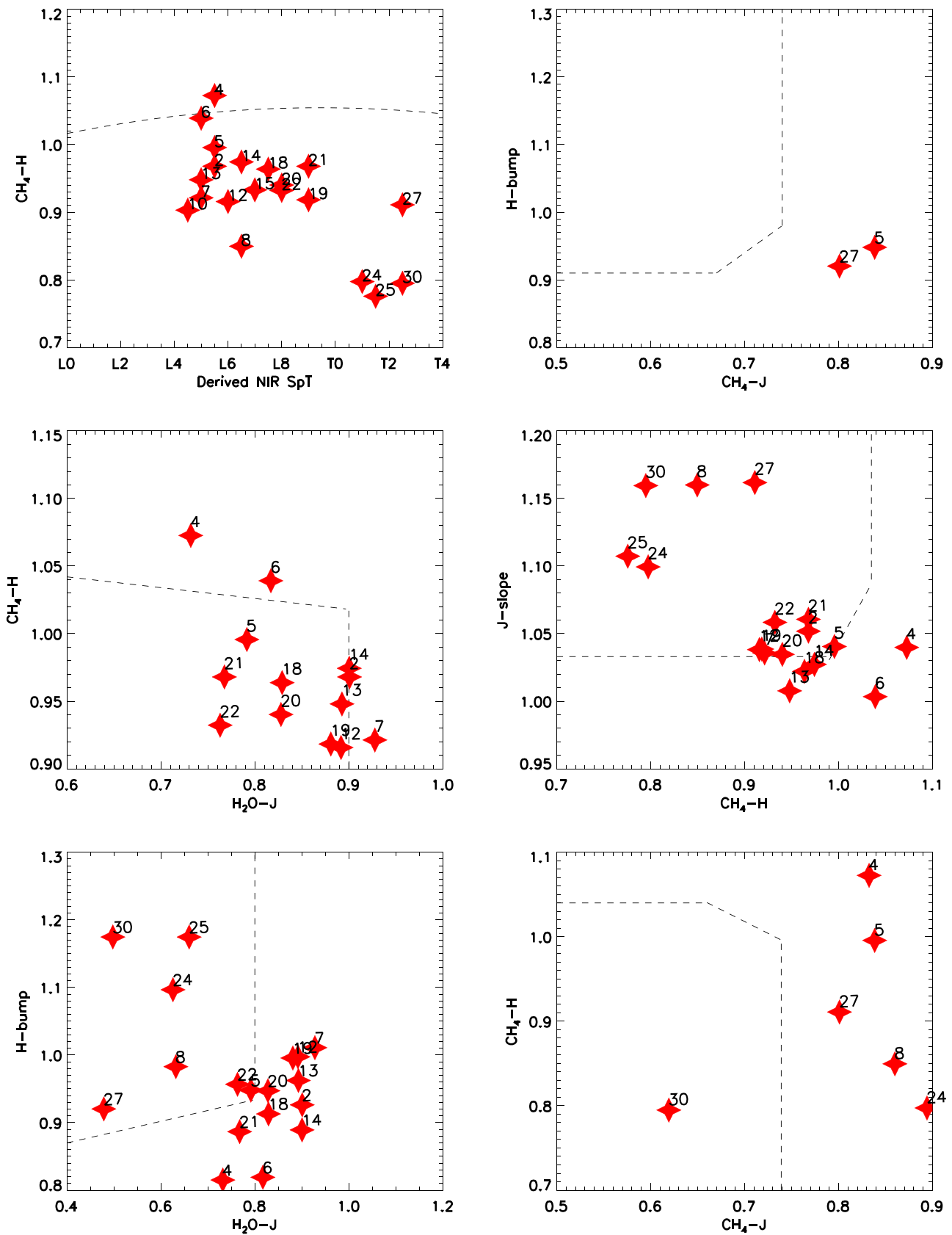


Figure 13. Spectral index selection. Numbers correspond to our objects. The boxes shown with dashed lines mark the areas where the selection criteria of Tables 15 and 16 are valid.

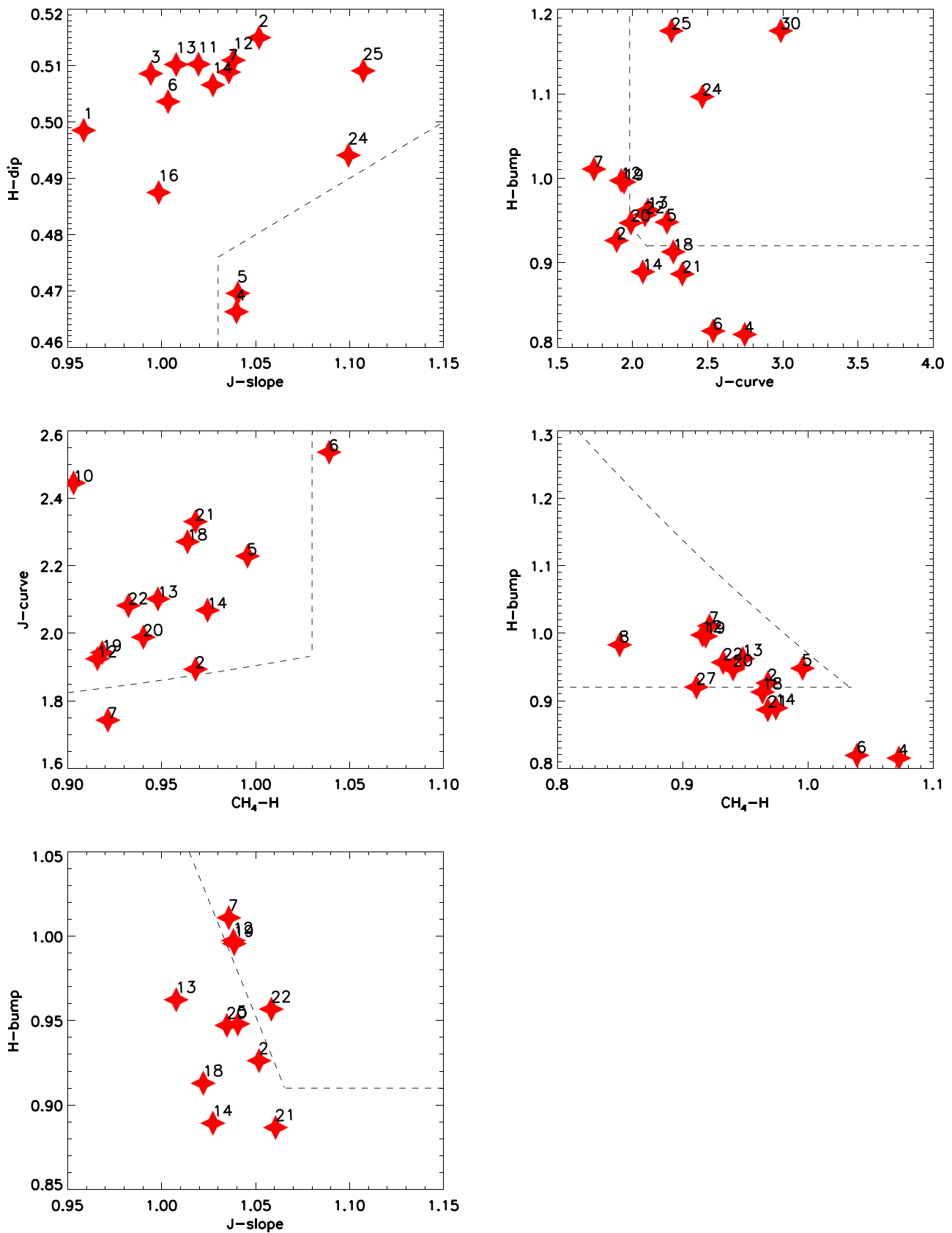



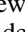




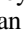

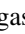
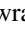


Figure 14. Spectral index selection. Numbers correspond to our objects. The boxes shown with dashed lines mark the areas where the selection criteria of Tables 15 and 16 are valid.

ORCID iDs

Elena Manjavacas  <https://orcid.org/0000-0003-0192-6887>
 Dániel Apai  <https://orcid.org/0000-0003-3714-5855>
 Yifan Zhou  <https://orcid.org/0000-0003-2969-6040>
 Ben W. P. Lew  <https://orcid.org/0000-0003-1487-6452>
 Glenn Schneider  <https://orcid.org/0000-0002-4511-5966>
 Stan Metchev  <https://orcid.org/0000-0003-3050-8203>
 Paulo A. Miles-Páez  <https://orcid.org/0000-0003-2446-8882>
 Mark S. Marley  <https://orcid.org/0000-0002-5251-2943>
 Nicolas Cowan  <https://orcid.org/0000-0001-6129-5699>
 Theodora Karalidi  <https://orcid.org/0000-0001-7356-6652>
 Adam J. Burgasser  <https://orcid.org/0000-0002-6523-9536>
 Patrick J. Lowrance  <https://orcid.org/0000-0001-8014-0270>

References

- Allard, F., Homeier, D., & Freytag, B. 2012, *RSPTA*, 370, 2765
 Aller, K. M., Liu, M. C., Magnier, E. A., et al. 2016, *ApJ*, 821, 120
 Allers, K. N., Gallimore, J. F., Liu, M. C., & Dupuy, T. J. 2016, *ApJ*, 819, 133
 Allers, K. N., & Liu, M. C. 2013, *ApJ*, 772, 79
 Andrei, A. H., Smart, R. L., Penna, J. L., et al. 2011, *AJ*, 141, 54
 Apai, D., Karalidi, T., Marley, M. S., et al. 2017, *Sci*, 357, 683
 Apai, D., Radigan, J., Buenzli, E., et al. 2013, *ApJ*, 768, 121
 Artigau, É., Bouchard, S., Doyon, R., & Lafrenière, D. 2009, *ApJ*, 701, 1534
 Bannister, N. P., & Jameson, R. F. 2007, *MNRAS*, 378, L24
 Bardalez Gagliuffi, D. C., Burgasser, A. J., Gelino, C. R., et al. 2014, *ApJ*, 794, 143
 Beatty, T. G., Madhusudhan, N., Tsiaras, A., et al. 2017, *AJ*, 154, 158
 Bedin, L. R., Pourbaix, D., Apai, D., et al. 2017, *MNRAS*, 470, 1140
 Benneke, B., & Seager, S. 2012, *ApJ*, 753, 100
 Biller, B. A., Vos, J., Bonavita, M., et al. 2015, *ApJL*, 813, L23
 Biller, B. A., Vos, J., Buenzli, E., et al. 2018, *AJ*, 155, 95
 Bonnefoy, M., Chauvin, G., Lagrange, A.-M., et al. 2014, *A&A*, 562, A127
 Borysow, A., Jorgensen, U. G., & Zheng, C. 1997, *A&A*, 324, 185
 Buenzli, E., Apai, D., Morley, C. V., et al. 2012, *ApJL*, 760, L31
 Buenzli, E., Apai, D., Radigan, J., Reid, I. N., & Flateau, D. 2014, *ApJ*, 782, 77
 Buenzli, E., Saumon, D., Marley, M. S., et al. 2015, *ApJ*, 798, 127
 Burgasser, A. J., Cruz, K. L., Cushing, M., et al. 2010, *ApJ*, 710, 1142
 Burgasser, A. J., Geballe, T. R., Leggett, S. K., Kirkpatrick, J. D., & Golimowski, D. A. 2006, *ApJ*, 637, 1067
 Burgasser, A. J., Kirkpatrick, J. D., Brown, M. E., et al. 2002, *ApJ*, 564, 421
 Burgasser, A. J.,Looper, D. L., Kirkpatrick, J. D., Cruz, K. L., & Swift, B. J. 2008, *ApJ*, 674, 451
 Burningham, B., Leggett, S. K., Homeier, D., et al. 2011, *MNRAS*, 414, 3590
 Burningham, B., Marley, M. S., Line, M. R., et al. 2017, *MNRAS*, 470, 1177
 Caballero, J. A. 2018, *Geosc*, 8, 362
 Cartier, K. M. S., Beatty, T. G., Zhao, M., et al. 2017, *AJ*, 153, 34
 Cruz, K. L., Kirkpatrick, J. D., & Burgasser, A. J. 2009, *AJ*, 137, 3345
 Cushing, M. C., Marley, M. S., Saumon, D., et al. 2008, *ApJ*, 678, 1372
 Cushing, M. C., Rayner, J. T., & Vacca, W. D. 2005, *ApJ*, 623, 1115
 Cutri, R. M., Skrutskie, M. F., van Dyk, S., et al. 2003, *yCat*, 2246, 0
 Dahn, C. C., Harris, H. C., Vrba, F. J., et al. 2002, *AJ*, 124, 1170
 Delorme, P., Schmidt, T., Bonnefoy, M., et al. 2017, *A&A*, 608, A79
 Deming, D., Wilkins, A., McCullough, P., et al. 2013, *ApJ*, 774, 95
 Dressel, L. 2019, *Wide Field Camera 3 Instrument Handbook*, Version 11.0 (Baltimore: STScI)
 Dupuy, T. J., & Liu, M. C. 2012, *ApJS*, 201, 19
 Evans, T. M., Sing, D. K., Kataria, T., et al. 2017, *Natur*, 548, 58
 Faherty, J. K., Burgasser, A. J., Walter, F. M., et al. 2012, *ApJ*, 752, 56
 Faherty, J. K., Rice, E. L., Cruz, K. L., Mamajek, E. E., & Núñez, A. 2013, *AJ*, 145, 2
 Fisher, C., & Heng, K. 2018, *MNRAS*, 481, 4698
 Fortney, J. J., Lodders, K., Marley, M. S., & Freedman, R. S. 2008, *ApJ*, 678, 1419
 Gagné, J., Burgasser, A. J., Faherty, J. K., et al. 2015a, *ApJL*, 808, L20
 Gagné, J., Faherty, J. K., Burgasser, A. J., et al. 2017, *ApJL*, 841, L1
 Gagné, J., Faherty, J. K., Cruz, K. L., et al. 2015b, *ApJS*, 219, 33
 Gaia Collaboration, Brown, A. G. A., Vallenari, A., et al. 2018, *A&A*, 616, A1
 Gandhi, S., & Madhusudhan, N. 2017, *MNRAS*, 472, 2334
 Gizis, J. E., Allers, K. N., Liu, M. C., et al. 2015, *ApJ*, 799, 203
 Gizis, J. E., Faherty, J. K., Liu, M. C., et al. 2012, *AJ*, 144, 94
 Hartig, G. F. 2009, *Instrument Science Report WFC3-2009-37* (Baltimore, MD: STScI)
 Haynes, K., Mandell, A. M., Madhusudhan, N., Deming, D., & Knutson, H. 2015, *ApJ*, 806, 146
 Herrero, E., Morales, J. C., Ribas, I., & Naves, R. 2011, *A&A*, 526, L10
 Home, K. 1986, *PASP*, 98, 609
 Hunter, J. D. 2007, *CSE*, 9, 90
 Kirkpatrick, J. D. 2005, *ARA&A*, 43, 195
 Kirkpatrick, J. D., Cushing, M. C., Gelino, C. R., et al. 2011, *ApJS*, 197, 19
 Kirkpatrick, J. D., Reid, I. N., Liebert, J., et al. 1999, *ApJ*, 519, 802
 Kirkpatrick, J. D., Reid, I. N., Liebert, J., et al. 2000, *AJ*, 120, 447
 Knutson, H. A., Benneke, B., Deming, D., & Homeier, D. 2014, *Natur*, 505, 66
 Kuntzschner, H., Kuemmel, M., Walsh, J., & Bushouse, H. 2009, *STECF*, 47, 4
 Kuntzschner, H., Kümmel, M., Walsh, J. R., & Bushouse, H. 2011, *ST-ECF Instrument Science Report WFC3-2011-05* (Baltimore, MD: STScI)
 Lavie, B., Mendonça, J. M., Mordasini, C., et al. 2017, *AJ*, 154, 91
 Lee, J.-M., Irwin, P. G. J., Fletcher, L. N., Heng, K., & Barstow, J. K. 2014, *ApJ*, 789, 14
 Leggett, S. K., Geballe, T. R., Fan, X., et al. 2000, *ApJL*, 536, L35
 Leggett, S. K., Tremblin, P., Esplin, T. L., Luhman, K. L., & Morley, C. V. 2017, *ApJ*, 842, 118
 Lew, B. W. P., Apai, D., Zhou, Y., et al. 2016, *ApJL*, 829, L32
 Line, M. R., Marley, M. S., Liu, M. C., et al. 2017, *ApJ*, 848, 83
 Line, M. R., Stevenson, K. B., Bean, J., et al. 2016, *AJ*, 152, 203
 Line, M. R., Teske, J., Burningham, B., Fortney, J. J., & Marley, M. S. 2015, *ApJ*, 807, 183
 Line, M. R., Wolf, A. S., Zhang, X., et al. 2013, *ApJ*, 775, 137
 Liu, M. C., Dupuy, T. J., & Allers, K. N. 2016, *ApJ*, 833, 96
 Liu, M. C., Magnier, E. A., Deacon, N. R., et al. 2013, *ApJL*, 777, L20
 Lothringer, J. D., Benneke, B., Crossfield, I. J. M., et al. 2018, *AJ*, 155, 66
 Luhman, K. L., & Esplin, T. L. 2016, *AJ*, 152, 78
 MacKenty, J. W., Kimble, R. A., O'Connell, R. W., & Townsend, J. A. 2010, *Proc. SPIE*, 7731, 77310Z
 Madhusudhan, N., Apai, D., & Gandhi, S. 2016, arXiv:1612.03174
 Madhusudhan, N., & Seager, S. 2009, *ApJ*, 707, 24
 Mamajek, E. E., & Bell, C. P. M. 2014, *MNRAS*, 445, 2169
 Mandell, A. M., Haynes, K., Sinukoff, E., et al. 2013, *ApJ*, 779, 128
 Manjavacas, E., Apai, D., Zhou, Y., et al. 2018, *AJ*, 155, 11
 Marley, M. S., Gelino, C., Stephens, D., Lunine, J. I., & Freedman, R. 1999, *ApJ*, 513, 879
 Marley, M. S., & Robinson, T. D. 2015, *ARA&A*, 53, 279
 Marley, M. S., Saumon, D., & Goldblatt, C. 2010, *ApJL*, 723, L117
 Marocco, F., Andrei, A. H., Smart, R. L., et al. 2013, *AJ*, 146, 161
 Marquardt, D. W. 1963, *SJAM*, 11, 431
 Marsh, K. A., Wright, E. L., Kirkpatrick, J. D., et al. 2013, *ApJ*, 762, 119
 Martin, E. C., Kirkpatrick, J. D., Beichman, C. A., et al. 2018, *ApJ*, 867, 109
 Martin, E. L., Rebolo, R., & Zapatero-Osorio, M. R. 1996, *ApJ*, 469, 706
 McLean, I. S., McGovern, M. R., Burgasser, A. J., et al. 2003, *ApJ*, 596, 561
 Metchev, S. A., Heinze, A., Apai, D., et al. 2015, *ApJ*, 799, 154
 Naud, M.-E., Artigau, É., Rowe, J. F., et al. 2017, *AJ*, 154, 138
 Parmentier, V., Line, M. R., Bean, J. L., et al. 2018, *A&A*, 617, A110
 Pecaut, M. J., & Mamajek, E. E. 2013, *ApJS*, 208, 9
 Peña Ramírez, K., Zapatero Osorio, M. R., & Béjar, V. J. S. 2015, *A&A*, 574, A118
 Pinhas, A., Rackham, B. V., Madhusudhan, N., & Apai, D. 2018, *MNRAS*, 480, 5314
 Radigan, J. 2014, *ApJ*, 797, 120
 Radigan, J., Jayawardhana, R., Lafrenière, D., et al. 2012, *ApJ*, 750, 105
 Radigan, J., Lafrenière, D., Jayawardhana, R., & Artigau, E. 2014, *ApJ*, 793, 75
 Rajan, A., Rameau, J., De Rosa, R. J., et al. 2017, *AJ*, 154, 10
 Ranjan, S., Charbonneau, D., Désert, J.-M., et al. 2014, *ApJ*, 785, 148
 Rasmussen, C. E., & Williams, C. K. I. 2006, *Gaussian Processes for Machine Learning* (Cambridge, MA: MIT Press)
 Sahlmann, J., Lazorenko, P. F., Bouy, H., et al. 2016, *MNRAS*, 455, 357
 Samland, M., Mollière, P., Bonnefoy, M., et al. 2017, *A&A*, 603, A57
 Schneider, A. C., Cushing, M. C., Kirkpatrick, J. D., et al. 2015, *ApJ*, 804, 92
 Sheppard, K. B., Mandell, A. M., Tamburo, P., et al. 2017, *ApJL*, 850, L32
 Shporer, A., O'Rourke, J. G., Knutson, H. A., et al. 2014, *ApJ*, 788, 92
 Stevenson, K. B., Bean, J. L., Madhusudhan, N., & Harrington, J. 2014a, *ApJ*, 791, 36
 Stevenson, K. B., Désert, J.-M., Line, M. R., et al. 2014b, *Sci*, 346, 838
 Swain, M., Deroo, P., Tinetti, G., et al. 2013, *Icar*, 225, 432
 Tinney, C. G., Burgasser, A. J., & Kirkpatrick, J. D. 2003, *AJ*, 126, 975

- Tinney, C. G., Faherty, J. K., Kirkpatrick, J. D., et al. 2014, *ApJ*, 796, 39
- Todorov, K. O., Line, M. R., Pineda, J. E., et al. 2016, *ApJ*, 823, 14
- Triaud, A. H. M. J. 2014, *MNRAS*, 439, L61
- Triaud, A. H. M. J., Lanotte, A. A., Smalley, B., & Gillon, M. 2014, *MNRAS*, 444, 711
- Varley, R., Tsiaras, A., & Karpouzas, K. 2017, *ApJS*, 231, 13
- Vrba, F. J., Henden, A. A., Luginbuhl, C. B., et al. 2004, *AJ*, 127, 2948
- Wahhaj, Z., Liu, M. C., Biller, B. A., et al. 2011, *ApJ*, 729, 139
- Wakeford, H. R., Sing, D. K., Evans, T., Deming, D., & Mandell, A. 2016, *ApJ*, 819, 10
- Wang, Y., Smart, R. L., Shao, Z., et al. 2018, *PASP*, 130, 064402
- Weinberger, A. J., Anglada-Escudé, G., & Boss, A. P. 2013, *ApJ*, 762, 118
- Wilkins, A. N., Deming, D., Madhusudhan, N., et al. 2014, *ApJ*, 783, 113
- Yang, H., Apai, D., Marley, M. S., et al. 2015, *ApJL*, 798, L13
- Yang, H., Apai, D., Marley, M. S., et al. 2016, *ApJ*, 826, 8
- Zhou, Y., Apai, D., Lew, B. W. P., & Schneider, G. 2017, *AJ*, 153, 243
- Zhou, Y., Apai, D., Metchev, S., et al. 2018, *AJ*, 155, 132
- Zuckerman, B., Song, I., & Bessell, M. S. 2004, *ApJL*, 613, L65
- Zuckerman, B., Song, I., Bessell, M. S., & Webb, R. A. 2001, *ApJL*, 562, L87